Guided Shear Horizontal (SH) Wave Electromagnetic Acoustic Transducer (EMAT) for In-line Nondestructive Inspection of Pipelines

Contract #: DTRS57-04-C-10053
Period of Performance: September 9, 2004 to March 9, 2005

Final Report

Presented to:

Mr. Merritt
Office of Pipeline Safety, DOT

Submitted by:
Intelligent Automation, Inc.
George Zhao, Gang Mei, Bulent Ayhan and Chiman Kwan

Oak Ridge National Lab
Venu Varma

Intelligent Automation, Inc.
15400 Calhoun Dr, Suite 400
Rockville, MD 20855

SBIR DATA RIGHTS

Contract No.: DTRS57-04-C-10053
Contractor Name: Intelligent Automation, Inc.
Contractor Address: 15400 Calhoun Drive, Suite 190, Rockville, MD 20855-2814
Expiration of SBIR Data Rights Period: 3/9/2010, unless extended by additional funding, in which case the SBIR Data Rights Period will expire 5 years following termination of such additional funding.

The Government's rights to use, modify, reproduce, release, perform, display, or disclose technical data or computer software marked with this legend are restricted during the period shown as provided in paragraph (b)(4) of the Rights in Noncommercial Technical Data and Computer Software--Small Business Innovative Research (SBIR) Program clause contained in the above identified contract. No restrictions apply after the expiration date shown above. Any reproduction of technical data, computer software, or portions thereof marked with this legend must also reproduce the markings.

DISTRIBUTION STATEMENT B:
Distribution Statement B: Distribution authorized to U.S. Government Agencies only; contains proprietary information.

Guided Shear Horizontal (SH) Wave Electromagnetic Acoustic Transducer (EMAT) for In-line Nondestructive Inspection of Pipelines

Phase 1 Final Report
Performance period: September 9, 2004 to March 9, 2005

Table of Contents

1. Phase 1 Summary 3
2. Review of Phase 1 Objectives and Technical Approach 5
2.1 Phase 1 Objectives 5
2.2 Phase 1 Technical Approach 6
2.2.1 SH Transducer: EMAT Sensor Principle and Design 6
2.2.2 Split-Spectrum Nonlinear Filter for Coherent Noise Reduction and Signal Extraction 8
2.2.3 Boundary Element Modeling of Guided Wave Interaction with Defects 9
2.2.4 Sensitive Algorithm for Defect Detection and Classification 11
3. Phase 1 Results 15
3.1 Theoretical modeling of SH wave incident into the dents using BEM Method 15
3.2 Defect Classification for man-made notch defects 18
3.3 “Cup” and “Saucer” Defect Detection, Classification, and Size Estimation for 12” Pipe 20
3.3.1 Mechanical dents creation and descriptions 21
3.3.2 EMAT data collection inside the 12-inch pipe 24
3.3.3 Defect Detection Based on Correlation Technique 27
3.3.4 PCA based Technique for Classification 28
3.3.5 Dent depth Estimation 29
3.4 Defect Detection and Classification for another 12” Pipe 30
3.5 Graphical User Interface for Demonstrations 32
4. Conclusions 33
5. Future Work 33
6. References 34
7. Appendices 35
7.1 Spectral Information Divergence (SID) [12] 35
7.2 Orthogonal Subspace Projection (OSP) [12] 35
7.3 Nonnegatively Constrained Least Squares Method (NCLS) [12] 36
7.4 ORNL EMAT PIG system SCC detection 37

1. Phase 1 Summary

Pipelines used for transporting natural gas and petroleum fluid are aging and may suffer from accidental damage. The need is growing for an efficient and reliable inspection system to locate and characterize the weak spots that can fail and result in leakage. Mechanical damage causes dents to be formed. For "saucer" dents which are smooth, it may not be critical; however, for "cup" dents that are abrupt, certain range of field conditions including soil type, stress, cathode potential, coating conditions, and temperature, etc., may lead it to a catastrophic failure. Axial and circumferential field magnetic flux leakage (MFL) In-Line Inspection (ILI) smart Pipe-Inspection-Gears (PIG) and compression wave ultrasonic transmission devices, currently used for detecting metal loss and other defects like Stress Corrosion Cracks (SCC), have the difficulty of reliably detecting the coincidental metal loss associated with the "cup" type injurious anomaly, let alone quantifying it.

If, instead of using the magnetic field and bulk wave ultrasound that are overly sensitive to the local surface condition, ultrasonic guided waves are directed through and along the wall of the pipe, flaws within the wave propagation path will reveal their unique signatures. By thoroughly analyzing the waveform collected from multi-sensors with multi-measurements at multi-locations, defect feature will be extracted and classified into various shape and sizes. This also reduces the impact of local unpredictable variations to the sensor arrays. Guided waves are elastic waves propagating along a thin walled structure or structural boundaries [1-3]. Shear Horizontal (SH) wave, a special type of guided wave whose particle displacement is parallel to the structure surface, has the advantage of simple wave structure, less mode conversion and less attenuation to fluid load and coating, etc. This makes it an ideal choice for defect detection in pipes.

In this project, Intelligent Automation, Incorporated (IAI) and Oak Ridge National Lab (ORNL) propose a novel and integrated approach to inspect the mechanical dents and metal loss in pipelines. It combines the state-of-the-art SH wave Electro-magnetic Acoustic Transducer (EMAT) technique, through detailed numerical modeling, data collection instrumentation, and advanced signal processing and pattern classifications, to detect and characterize mechanical defects in the underground pipeline transportation infrastructures. The technique has four components: (1) thorough guided wave modal analysis, (2) recently developed three-dimensional (3-D) Boundary Element Method (BEM) for best operational condition selection and defect feature extraction, (3) ultrasonic Shear Horizontal (SH) waves EMAT sensor design and data collection, and (4) advanced signal processing algorithm like nonlinear split-spectrum filter, Principal Component Analysis (PCA) and Discriminant Analysis (DA) for signal-to-noise-ratio enhancement, crack signature extraction, and pattern classification. This technical not only can effectively address the problems with the existing methods, i.e., to detect the mechanical dents and metal loss in the pipelines consistently and reliably, but also it is able to determine the defect shape and size to certain extent. The key advantages of our proposed approach are summarized in the next few paragraphs:

- Sensitive SH wave to inspect various defects in the pipeline
  An SH wave propagates in a pipe structure with its energy distributed across the pipe wall. It can detect cracks and corrosions anywhere along its traveling path. Since the particle displacement of an SH wave is parallel to the pipe surface, it is less sensitive to the surface condition, has less mode conversion at the defects, and the interpretation of signals is easier as compared to other types of guided wave such as Lamb waves [3]. This capability enables us to inspect both the inner surface and outer surface of the pipe wall for metal loss with an ILI SH EMAT PIG setup easily and rapidly.

- Computationally efficient BEM model to optimally determine the working conditions of SH EMAT PIG
  The eigen-modes of SH waves span all the wave-number vs. frequency domain represented by dispersion curves [4]. To select the optimal mode and frequency for best inspection sensitivity, a BEM model will be set up to emulate the SH wave interaction with a crack in the pipe. By extensive parametric study of the wave scattering factors vs. wave mode and frequency, the best combination can be determined for metal loss detection. Since the "cup" dents and buckles are three dimensional defects, a 3-D numerical model is required for this problem. BEM has the advantage of dimensionality reduction, less computer time and storage, more targeted calculation etc. over the popular Finite Element Method (FEM) [5-6]. It is used for the guided wave scattering problem. The PI of this proposal has extensive experience in BEM model and has developed 2-D and 3-D code for the SH wave defect characterization.

- Non-contact, couplant free EMAT to generate and receive SH waves
  The use of EMAT to generate and receive SH waves is another advantage. EMAT works on the principle of Lorentz force in non-ferromagnetic materials like aluminum and copper etc., and Lorentz force combined with magnetostrictive effect in ferromagnetic materials like nickel and steel. One big advantage of these electromagnetic energy transduction methods is the non-contact properties. The absence of liquid couplant makes EMATs a primary choice for operating at elevated temperatures and for high speed scanning. Furthermore, the

operation characteristics of EMATs can be reproduced from one unit to another quite easily since they are only made of a piece of conducting wire and a permanent magnet; and the test results of EMATs are highly stable and repeatable. Another important feature of EMATs is it can generate SH waves efficiently, which must otherwise be generated with piezoelectric transducers rigidly bonded or sticky coupling to the pipe wall. The PI of this proposal has designed and manufactured various EMAT probes, including SH and Lamb wave EMAT, for both Penn State University and the Oak Ridge National Lab.

- Proven signal processing algorithms to extract weak signatures and characterize defect
  Due to the coating and underground burying nature of the pipelines, as well as the EMAT sensor noise during the scanning process, the waveform signature from the defects will be extremely weak. After the waveforms are collected, a signal processing algorithm called split-spectrum [7] filter will be used to improve the signal-to-noise ratio. Then the PCA will be applied to extract the crack signatures features out of the mixed acoustic signals. From a wave feature B-scan image, or by using a pattern classifier such as Discriminant Analysis, the presence of mechanical dents can be determined. PCA is a linear neural network. A key benefit is that it significantly reduces the input data dimensionality. The specific algorithm for this project includes windowing the time domain waveform corresponding to the effective inspection area by transforming into the frequency domain, and then using the PCA network for metal loss determination. IAI has applied PCA and DA in many applications such as waveform recognition for the Space Shuttle, helicopter gearbox failure classification, diagnostics for the Call Processing Component of the Iridium 66 satellite worldwide telephony system, etc.

In Phase 1, we have achieved many significant results. Fig. 1 summarizes our major achievements. First, we performed theoretical studies and BEM simulations on the impact of Shear Horizontal guided waves to defects in pipes. The study shows that the transmission coefficient and resultant waveform changes are useful features that will guide us in frequency and mode selections for better defect detection. Second, several algorithms have been implemented for defect classification. Third, various defects such as notch crack, “cup”, and “saucer” dents were produced on a steel pipe and SH wave data were collected on these defect with a pair of EMATs. Fourth, extensive data analysis was carried out and it was found that the PCA-DA algorithm yielded very good performance: we were able to detect and classify dents with size as small as 0.1”, which is much smaller than the safety requirements (0.5”) that OPS listed for a 12-inch standard seamless pipe. Fifth, a Graphical User Interface (GUI) was designed and implemented for the SH EMAT inspection system which will assist inspection of the pipelines. User can select any raw data files from normal, “cup”, and “saucer” cases, and the signal are displayed along with the detection and classification results so that a user can get first-hand information about the performance of the algorithm. This GUI can be further improved in phase 2 for automatic defect detection and classifications.

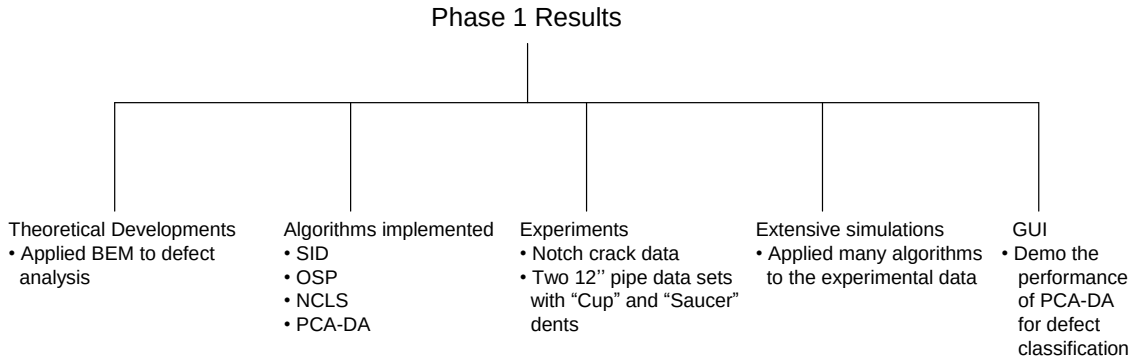

Fig. 1 Summary of Phase 1 results.

2. Review of Phase 1 Objectives and Technical Approach

2.1 Phase 1 Objectives

After the project started, we set up a kick-off meeting with Mr. Merritt of OPS. From the meeting and several correspondences afterwards, we were able to refine our task plans. More importantly, we learned that seamless pipes cause more problem for defect inspection than the roll-welded pipes. The wall thickness of the seamless pipe could vary up to 10% and it is periodic with a wavelength about 1 foot. The variation of a seamed pipe is less than 2%. We believe this variation will not affect the EMAT signal much, but will take that into account for signal processing and defect classification stages. For the Phase 1 project, we will stick to 12" pipe and do all the preliminary proof-of-principle demonstration. Once we are in Phases 2 or 3, we can figure out how it needs to be integrated. When the pipe diameter changes, all the fixtures change. Some modifications are needed to accommodate for the mechanical damages that the PIG will encounter when going through the pipe. Since the lift off will be of concern when the EMATs pass though the pipe, we need to make a careful mechanical design.

Based on the OPS pipeline safety regulation 49 CFR Part 192 pipeline Safety: Pipeline Integrity Management in High Consequence Areas (Gas Transmission Pipelines). The proposed rule is that a dent with a depth greater than 6% of the pipeline's diameter (greater than 0.5 inch for a pipeline diameter less than Nominal Pipe Size 12) or a dent with a depth greater than 2% of the pipeline's diameter (0.25 inch for a pipeline diameter less than NPS 12) that affects the pipe curvature at girth weld and longitudinal seam weld, needs a 180-day remediation. Our man-made dents should be shallower than the case mentioned above which means less than 0.25 inch for 12" pipe and less than 0.6 inch for the 30" pipe. Table 1 lists the proposed dent size and shape for Phase 1 research.

Table 1: Specifications of the dent dimensions to be introduced to the 12" pipe

Dent Type	Diameter of Ball	Depth	Dent diameter
Saucer	3.75	0.25	2
	3.75	0.156	1.5
	4.8	0.2	2
	4.8	0.35	2.5
Cup	1	0.5	1
	1	0.4	0.98
	0.75	0.375	0.75
	0.75	0.3	0.375

The specific method to introduce dent defect on a pipe is to use hydraulic press machine, with various sizes of ball-heads pressing onto the outer surface of the pipe wall. ORNL has the facility in producing these defects.

Our key Phase 1 objective is to demonstrate that our proposed system can detect and classify defects with size smaller than 0.25" for 12" pipes. Through many experiments and simulations, we have clearly demonstrated the feasibility of our system. Section 3 summarizes our results in detail.

2.2 Phase 1 Technical Approach

The proposed system architecture is shown in Fig. 2. SH wave EMAT sensors are placed inside a pipe on a test fixture that can be pulled through the pipe. The EMAT sensor is optimally designed with the best sensitivity to the dents and metal loss in the pipe. The tone-burst signal, whose frequency is also optimized with BEM, is input to the EMAT. The scattered ultrasonic signal from defects will be captured by all the EMAT and digitized by Data Acquisition Card (DAC) with filtering and noise reduction, the data are sent to PCA network for flaw feature extraction and LVQ classifier or B-scan imaging system for display.

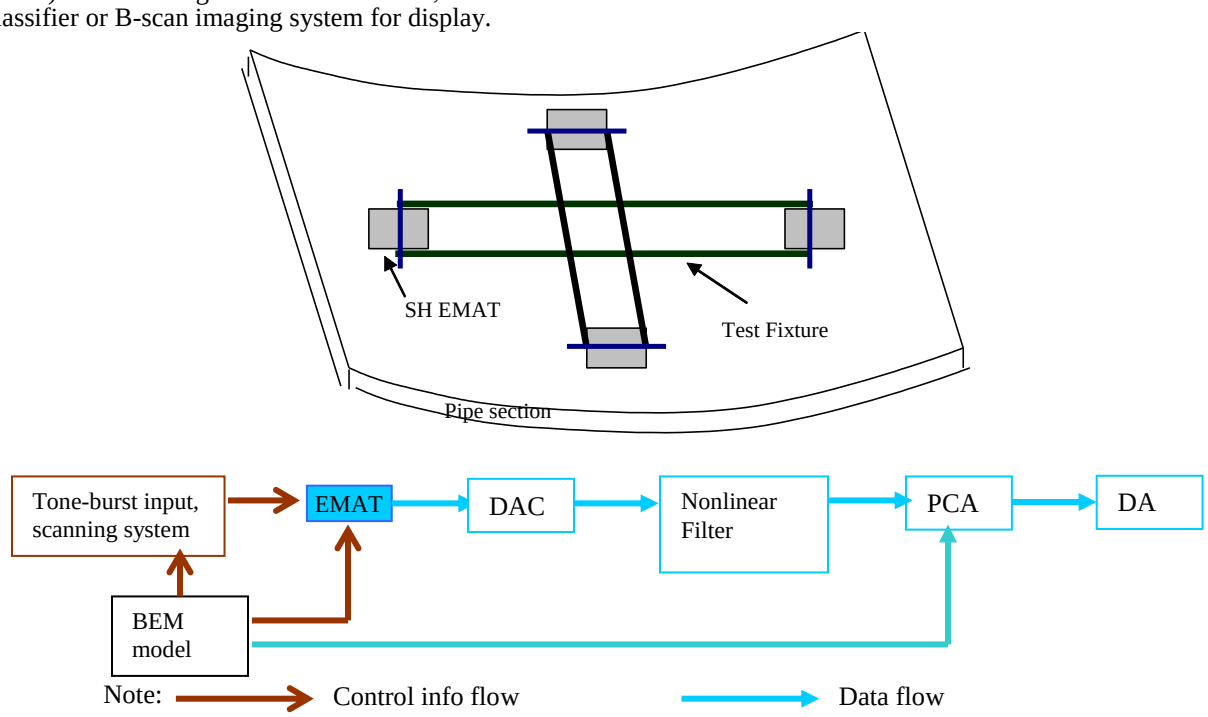

Fig. 2 Architecture of the proposed in-line pipe inspection system

The use of guided SH wave is both an art and a technology. The benefit of the above proposed approach includes:

- Long range inspection capability of SH waves from a single probe position.
- Insensitive to the liquids transporting inside the pipe or the protecting coating layer and soil outside.
- Optimized probe design and inspection parameters with a solid BEM modeling.
- Renovated nonlinear filter for extracting flaw signal which may totally buried under the noise even after linear filtering and waveform time averages.
- Robust and sensitive fault diagnosis algorithm with PCA and DA, and versatile result output capability.
- Compatible and easy integration with existing ILI system.

Details of each module are summarized below.

2.2.1 SH Transducer: EMAT Sensor Principle and Design

For a 12-inch diameter standard pipe, the dispersion curves of the circumferential SH wave is shown in Fig. 3. In our study, n_1 mode SH wave was used due to its high excitation and reception efficiency compared with the n_0 mode.

The basic components of EMAT consist of a face coil and magnets. It works under the Lorentz force principle in a non-ferromagnetic metal. The oscillating current in the face coil induces oscillatory eddy current at the surface of a metal close to the face coil. Under the magnetic field of the permanent magnets or electromagnets, the induced eddy current will exert vibration force to the lattice of metal microstructure, which in turn induces mechanical vibration in the material. The EMAT receiver is just the reverse of that process. It is of a great advantage that EMAT does not require couplant for transmitting energy into the material like conventional piezoelectric transducers. And it can be easily put onto and taken off from the structure and has very good measurement repeatability. Fig. 4 shows the diagram of the SH EMAT principle and a sample SH EMAT probe. The length of the alternating magnets in the wave propagation direction determines the slope of the excitation line that runs from the origin across the dispersion curve (see Fig. 3 dashed line), i.e.

$$\lambda = 2d = \frac{C_p}{f} \tag{2}$$

where λ is the wavelength of the SH wave to be generated, d is the distance between the center of the two adjacent alternating magnets, C_p is the phase velocity and f is the excitation frequency.

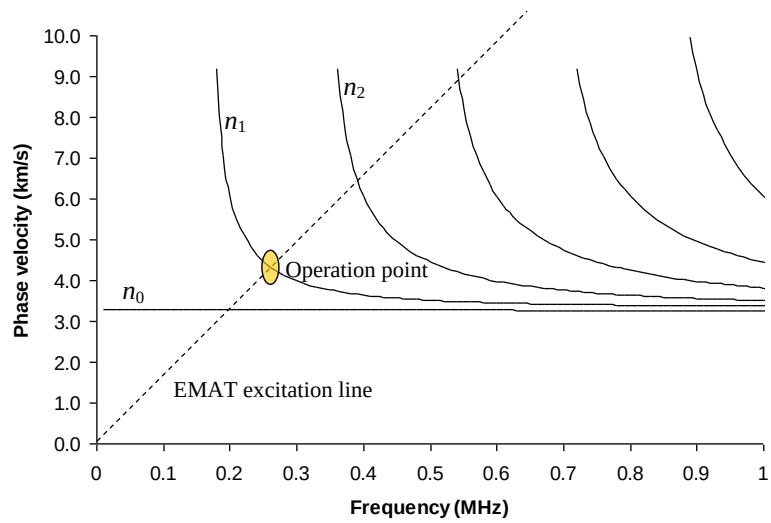

Fig. 3 Circumferential SH wave dispersion curves in a 12-inch standard pipe.

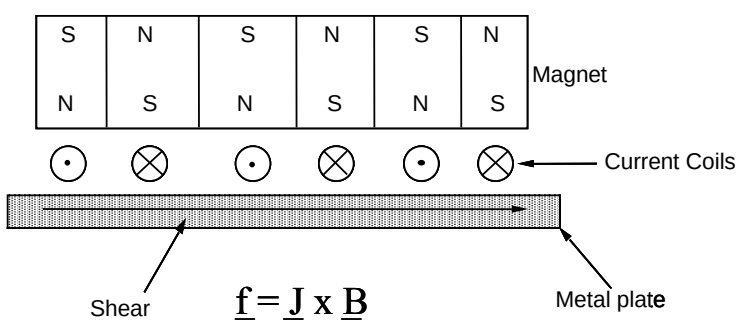

(a)

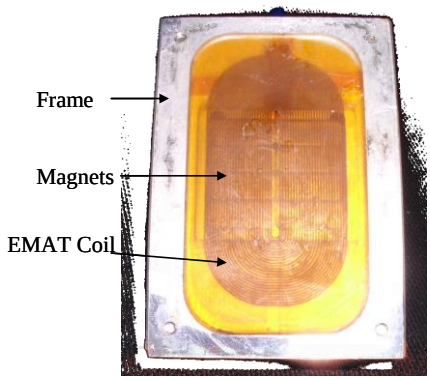

(b)

Fig. 4 (a) Principle of the Lorentz force SH wave EMAT and (b) SH EMAT probe designed for this study.

Fig. 5 (a) shows a 270 kHz EMAT system we produced at IAI, which consists of an EMAT transmitter, a receiver, impedance-matching networks and a signal amplifier. A sampled through-transmission signal on a 2mm aluminum plate is shown in Fig. 5 (b), which demonstrated good S/N ratio. We expect no problem producing a specialized probe for this project.

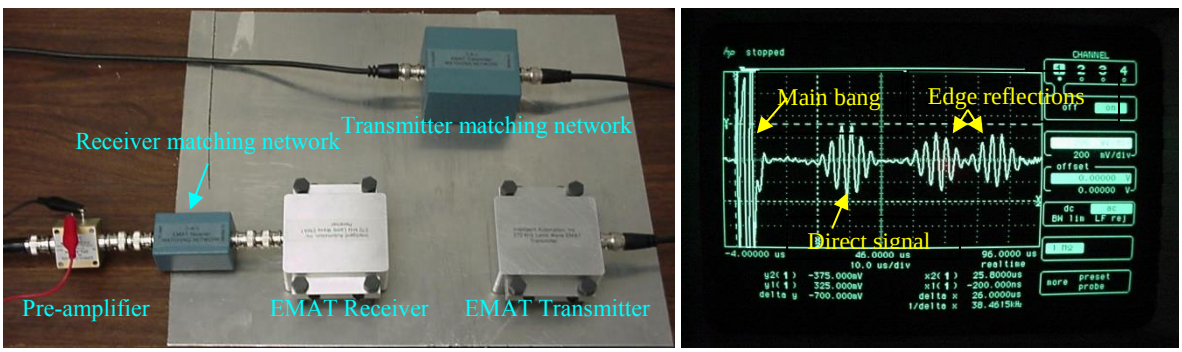

Fig. 5 (a) an example EMAT sensor system made at IAI and (b) EMAT signal of the test shown in (a)

2.2.2 Split-Spectrum Nonlinear Filter for Coherent Noise Reduction and Signal Extraction

For ILI of pipelines, noise is usually a big issue that can deteriorate the effectiveness of the inspection. if noise if random and time-dependent, a simple time averaging or temporal compounding is usually sufficient to improve the signal to noise ratio (SNR). However, for noise that is coherent (time-invariant), conventional linear filtering or time average failed to eliminate the noise. Recently, we have renovated a split-spectrum nonlinear filtering algorithm can shows great success in extracting useful signal out of overwhelmingly coherent noises. The technique makes use of the frequency domain spectrum of the raw data by spiting it into tens of separate spectrum channels with overlapping Gaussian windows. By taking the minimization and polarity thresholding functions on the spectrum channels and merging into a single spectrum, the inverse Fourier transformed signal will retain only the flaw signal while eliminate the noise.

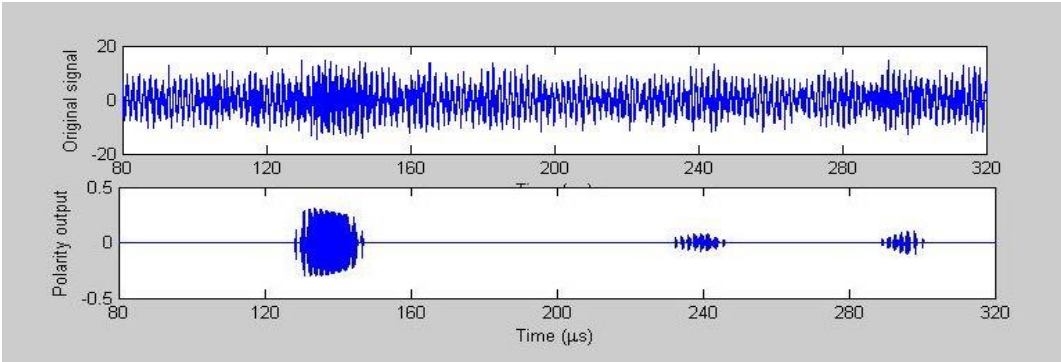

Fig. 6 An example of the split-spectrum noise reduction for an ultrasonic raw waveform

The top plot of Fig. 6 is the raw data collected from a 3 MHz Lamb wave sensor for crack detection in a plate by using Metac TB-1000 toneburst card. The signal is already bandpass filtered (500 kHz~ 5MHz), and time-averaged 100 times. The signal is seen buried under the noise. Conventional linear filters and wavelet denoising approach did not work for this data.

Showed on the bottom is the post-processed crack signature with our newly developed nonlinear filtering. The first big signal is the echo from the crack. The other two are verified to be an edge reflection and another lamb wave mode. The noise is totally eliminated while the defect signal is extracted

2.2.3 Boundary Element Modeling of Guided Wave Interaction with Defects

The basic idea of using BEM to simulate guided wave interaction with defects is to provide a guideline for defect shape and size estimation in a plate or pipe structure without much experimental effort. BEM has the advantage of much better computational efficiency over the more popular Finite Element Method (FEM) for the same accuracy. It only meshes the boundary of the domain instead of the whole domain area (Fig. 7 (a)). Fig. 7 (b) is an example of using SH wave to size a crack and corrosion type of defect in a steel plate [8]. The calculated reflection and transmission coefficients of n_0 mode SH wave from the three different shaped defects are shown in Fig. 8, in which it is seen that at low frequency the reflection coefficient increases monotonically and transmission coefficients deceases monotonically with the increase of defect size. For narrow surface crack or notch, this tread extends to the whole frequency covered in the computation. Generally speaking, for the specimens considered, SH wave around 100 kHz has the best sensitivity for defect detection using reflected signals. Fig. 9 shows the experimental verification of the results using 220 kHz EMAT probes. Good agreement was obtained. For the problem in this proposal, BEM model could easily be modified to take the plate taper angle into account. Our software has the capability to model stepped, tapered or lap-jointed cross-sectional waveguide by changing the geometry mesh input.

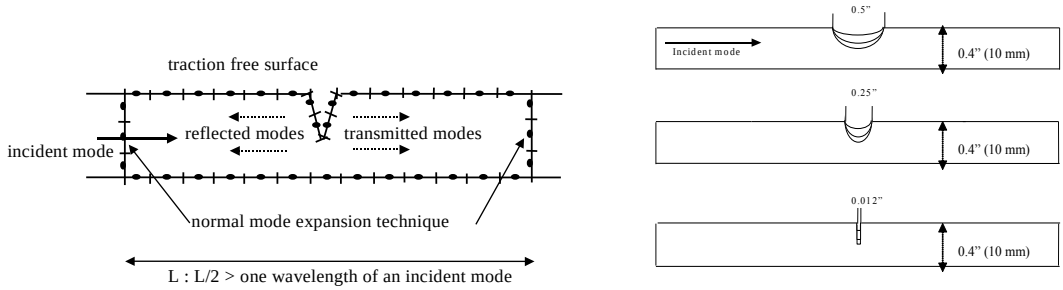

(a) (b)

Fig. 7 (a) Boundary element mesh for evaluating guided wave scattering from a surface–breaking defect; (b) Sample plates with defects of three different shapes and of 10%, 20%, … 90% through plate thickness.

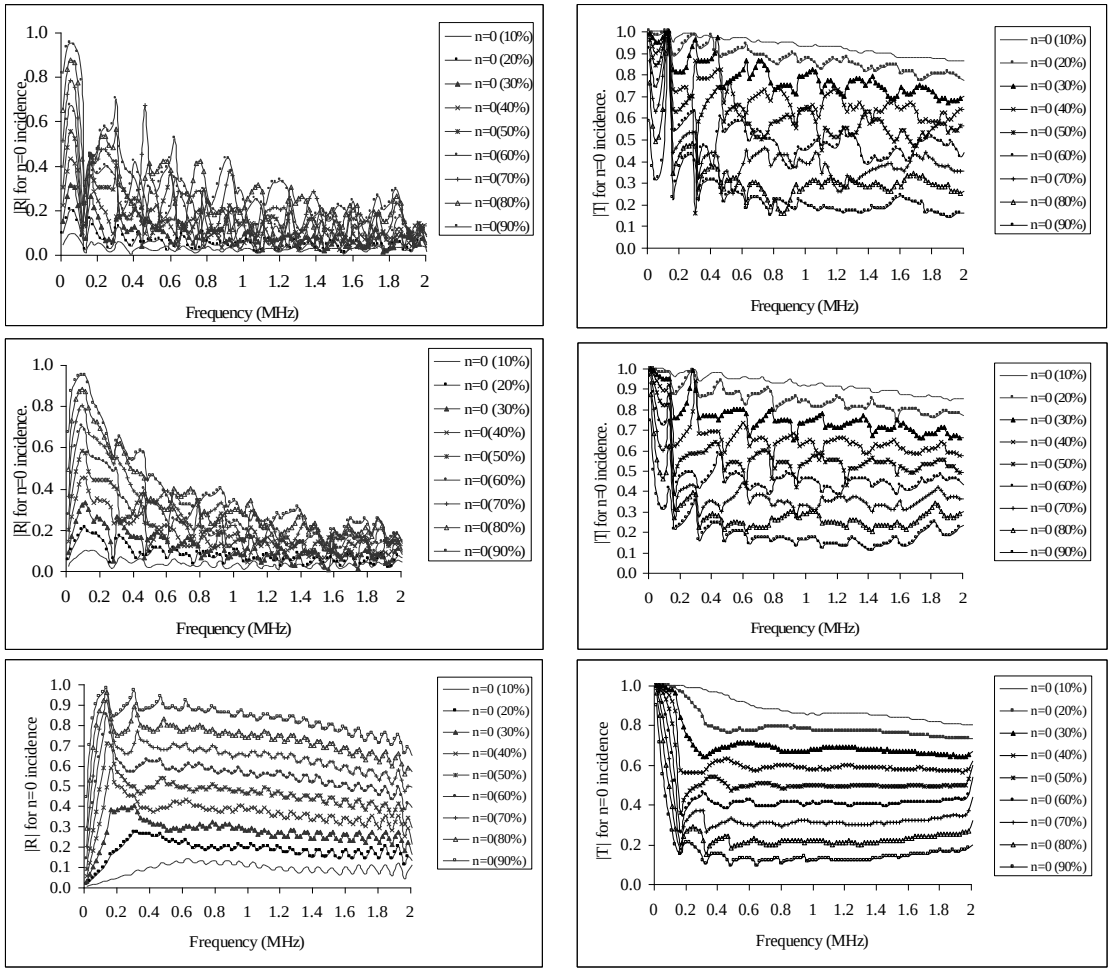

Fig. 8 From top to bottom, approximated reflection and transmission coefficients for n_0 mode SH wave incident into a 0.5”, 0.25” and 0.012” surface opening elliptical defects with 10%, 20%, .., 90% through plate thickness depth.

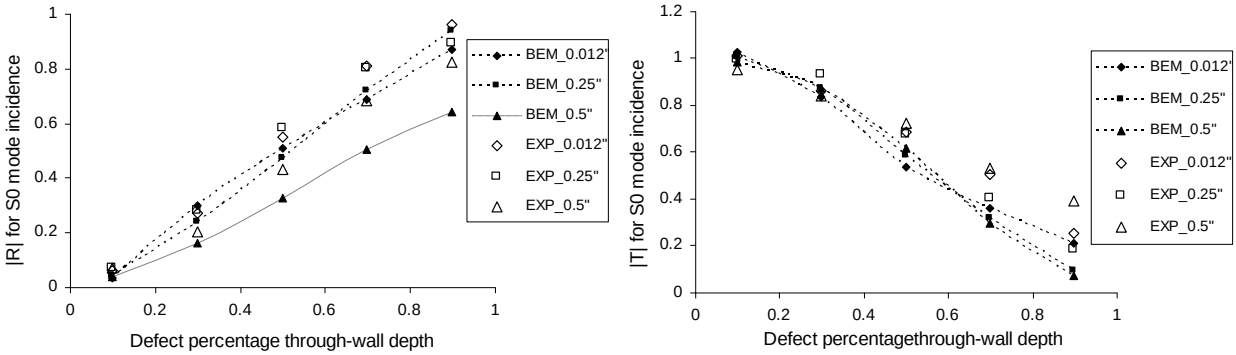

(a) (b)

Fig. 9 Theoretical and experimental comparison of (a) Reflection and (b) Transmission coefficients for 210 kHz n_0 mode SH wave incident into a 0.012” (0.3mm), 0.25” (6.35mm) and 0.5” (12.7mm) elliptical defect with 10%, 30%, … 90% through plate thickness.

To investigate the effect of a 3-D shape to the scattering pattern in the angular direction in the pipe, a 3D BEM model can be setup [9]. Fig. 10 shows a schematic view of the model, where the boundary of a virtual region enclosing a realistic defect (e.g. a circular through plate hole) was meshed with quadrilateral elements. A time-harmonic plane SH wave is incident onto the defect. The scattered wave fields were decomposed as a superposition of various circular

crested eigen-modes of both Lamb wave and SH waves [9]. The wave displacement and stress fields are then calculated in different directions and form an angular pattern. For different defects, this pattern is expected to be different, which could be used for defect shape and sizing analysis. Fig. 11 shows a sampled result when a 0.8MHz SH wave incident onto the circular hole. The diameter of the hole is the same as the thickness of the plate. The displacement amplitude at 10 times the radius around the hole is plotted for both the SH wave mode and mode converted Lamb modes, which shows that for SH modes, most of the energy is either reflected back or transmitted through the defect.

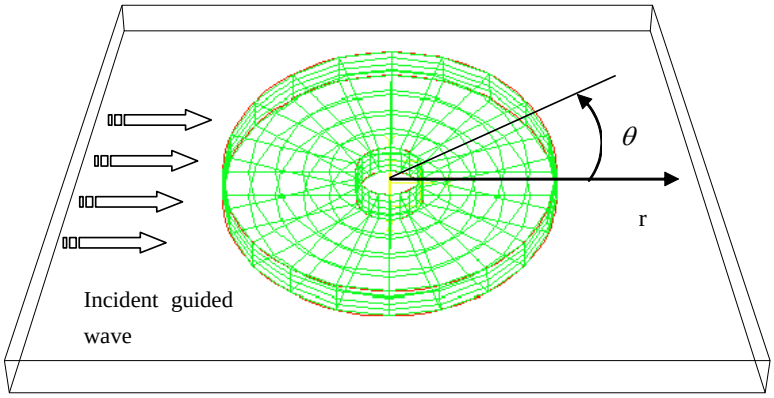

Fig. 10 A schematic problem of a plane guided wave incident into a three-dimensional defect in an infinite plate.

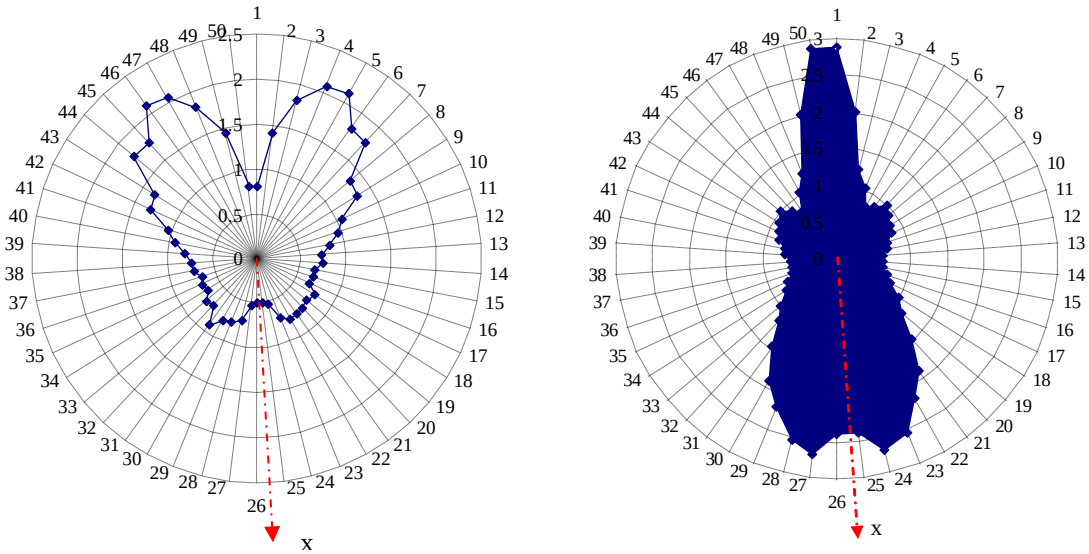

Fig. 11 The scattered (a) S_0 mode Lamb wave and (b) n_0 mode SH wave particle displacement amplitude on the virtual cylindrical boundary for 0.8 MHz n_0 mode SH wave incidence.

2.2.4 Sensitive Algorithm for Defect Detection and Classification

In this section, the PCA-DA algorithm is briefly introduced for its formulas, process steps, etc. the block diagram is as shown in Fig. 12. The major steps are listed below.

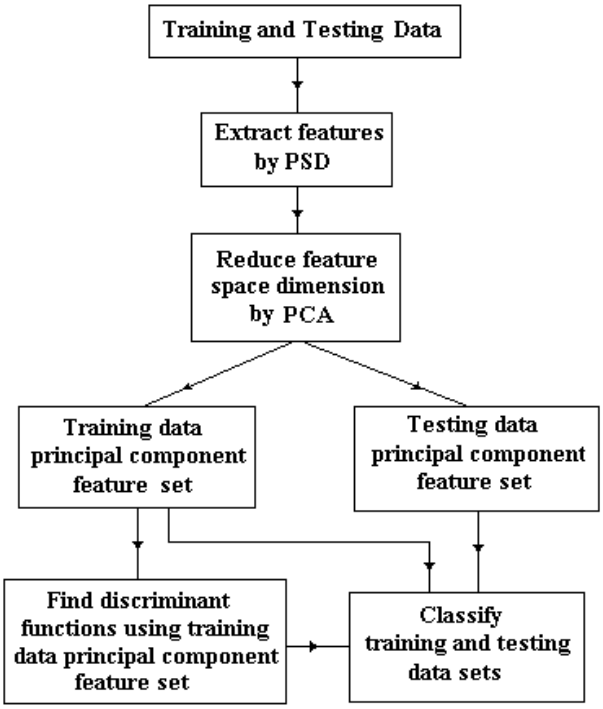

Fig. 12 Block diagram of the PCA-LDA based classification method.

Feature Extraction by PSD (Power Spectral Density)

The features used in the classification are extracted by one of the Power Spectral Density methods: Periodogram. Fig. 13 depicts the PSD of the training and testing data sets between frequencies 80 and 170 (frequency in samples).

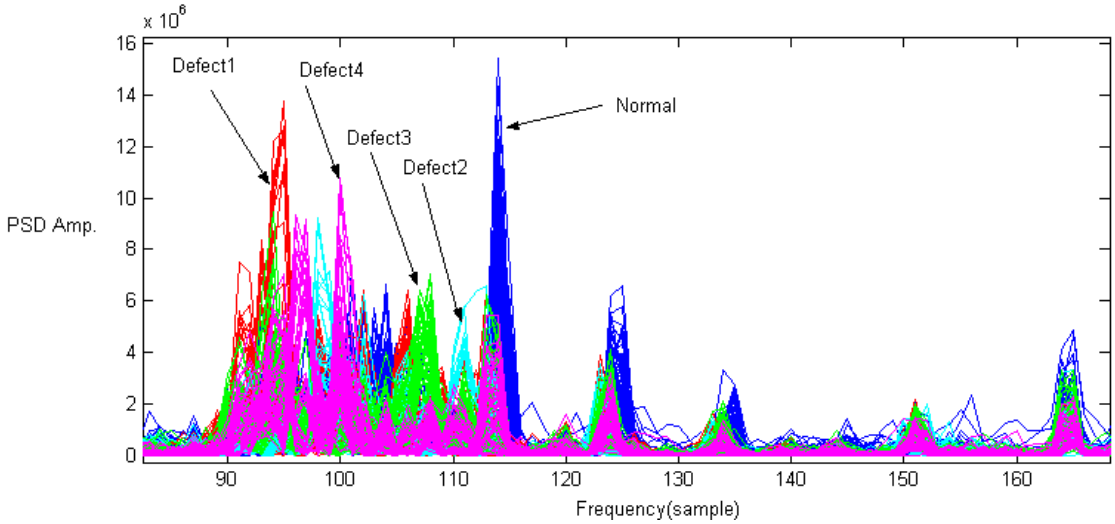

Fig. 13 PSD waveforms of the experimental data set (periodogram method).

Feature Dimension Reduction by PCA (Principal Component Analysis)

The dimension of the feature space is reduced by applying PCA. In this way, only the principal component features are included in the classification process. The PCA is a well-known and widely used dimension reduction technique [10].

In PCA, first the mean vector, $\boldsymbol{\mu}$, and the covariance matrix, $\boldsymbol{\Sigma}$, are computed for the full data set. In our case, the data set corresponds to the spectrum data vectors obtained from PSD. Next the eigenvectors and the eigenvalues are computed. The eigenvalues are sorted in a descending order. Finally, a matrix **A**, whose columns consist of the *k* eigenvectors with the largest eigenvalues is formed. The data is then projected onto the *k*-dimensional subspace in order to represent the data by principal components.

<u>Classification with DA (Discriminant Analysis)</u>

Suppose there is a set of *n* dimensional samples, $\mathsf{D} = \{\mathbf{x}_1, ..., \mathbf{x}_N\}$, where each data sample is represented by a data vector, $\mathbf{x}_j$. The samples in D belong to a total of *c* classes and D_i will be used as the notation to represent the data samples in class i, where $i = 1, ..., c$. Let $\mathbf{m}_i$ represent the class mean, and n_i represent the number of samples in class i. The relation between within-class scatter matrix and scatter matrices can then be depicted by (1).

$$\mathbf{S}_W = \sum_{i=1}^{c} \mathbf{S}_i \ , \tag{1}$$

where, the scatter matrices can be expressed by (2).

$$\mathbf{S}_i = \sum_{\mathbf{x} \in \mathsf{D}_i} (\mathbf{x} - \mathbf{m}_i)(\mathbf{x} - \mathbf{m}_i)^t \ . \tag{2}$$

The class mean and total mean vectors can be depicted as (3) and (4), respectively.

$$\mathbf{m}_i = \frac{1}{n_i} \sum_{\mathbf{x} \in \mathsf{D}_i} \mathbf{x} \, , \tag{3}$$

$$\mathbf{m} = \frac{1}{n} \sum_{\mathbf{x}} \mathbf{x} = \frac{1}{n} \sum_{i=1}^{c} n_i \mathbf{m}_\mathbf{i} \ . \tag{4}$$

With these definitions the total scatter matrix, and between class scatter matrices are introduced in (5-7).

$$\mathbf{S}_T = \sum_{\mathbf{x}} (\mathbf{x} - \mathbf{m})(\mathbf{x} - \mathbf{m})^t \ , \tag{5}$$

$$\mathbf{S}_B = \sum_{i=1}^{c} n_i (\mathbf{m}_i - \mathbf{m})(\mathbf{m}_i - \mathbf{m})^t \, , \tag{6}$$

$$\mathbf{S}_T = \mathbf{S}_W + \mathbf{S}_B \, . \tag{7}$$

The LDA based classifier is based on computing the *c* discriminants for the given *c* classes in the data set. In the computation of the discriminant functions within this classifier, it will be assumed that the covariance matrices of each class, $\boldsymbol{\Sigma}_i$, are different, and $\boldsymbol{\mu}_i$ is the vector corresponding to the mean of each class. The resulting discriminant functions are quadratic, and mathematically described in (8):

$$g_i(\mathbf{x}) = \mathbf{x}^t \mathbf{W}_i \mathbf{x} + \mathbf{w}_i^t \mathbf{x} + w_{i0} \, , \tag{8}$$

where $\mathbf{W}_i$ is mathematically introduced in (9), $\mathbf{w}_i$ in (10), and ω_{i0} in (11):

$$\mathbf{W}_i = -\frac{1}{2} \boldsymbol{\Sigma}_i^{-1} \, , \tag{9}$$

$$\mathbf{w}_i = \boldsymbol{\Sigma}_i^{-1} \boldsymbol{\mu}_i \, , \tag{10}$$

$$\omega_{i0} = -\frac{1}{2} \boldsymbol{\mu}_i^t \boldsymbol{\Sigma}_i^{-1} \boldsymbol{\mu}_i - \frac{1}{2} \ln \left| \boldsymbol{\Sigma}_i \right| + \ln P(\omega_i) \, . \tag{11}$$

Note that in (11), $P(\omega_i)$ represents the prior probability of each class. However, in this study it is assumed that each class has the same prior probability. There are *c* discriminant functions, where $g_i(x)$ denotes the discriminant function for class i. The class label of sample x is determined by comparing the magnitudes of the *c* discriminant functions with respect to *x*, and the maximum value among them determines the class decision as depicted in (12).

$$\arg\max_i (g_i(x)) \,. \tag{12}$$

Computation of MER (Modeling Error Rate)

The objective of PCA is to reduce the number of features, while still providing enough information about the data. The number of principal components can be determined by examining the modeling error rate, *MER*. In order to express the modeling error rate, the following nomenclature is introduced in the following:

Nomenclature:

$\mathbf{x}_k$: k^{th} feature vector, $k = 1, ..., n$

n : number of feature vectors

d : dimension of $\mathbf{x}$

$\mathbf{m}$: mean of $\{\mathbf{x}_k\}_{k=1}^{n}$

d' : reduced dimension number, $d' < d$

$\mathbf{e}_i$: eigenvectors of the scatter matrix with the largest eigenvalues, $i = 1, ..., d$

a_{ki} : i^{th} principal component for the kth feature vector, where $i = 1, ..., d$, and $k = 1, ..., n$

J_d : error criterion for $\{\mathbf{x}_k\}_{k=1}^{n}$ with a reduced dimension of d'

The modeling error rate (in percentage), *MER*, is then mathematically expressed as

$$MER(\%) = \frac{J_{d'}}{\sum_{k=1}^{n} \|\mathbf{x}_k\|^2} \times 100 \,, \tag{13}$$

where $J_{d'} = \sum_{k=1}^{n} \left\| \left(\mathbf{m} + \sum_{i=1}^{d'} a_{ki} \mathbf{e}_i \right) - \mathbf{x}_k \right\|^2$.

3. Phase 1 Results

In Phase 1, we have performed many experiments and applied quite a few algorithms to evaluate the pipeline health status. Data from three separate experiments were used to validate the performance of our overall technical approach.

3.1 Theoretical modeling of SH wave incident into the dents using BEM Method

In this study, boundary element modeling (BEM) is set up for calculating the reflection and transmission coefficients of SH wave impinging onto the dent defects. A two dimensional model is setup, with the "cup" and "saucer" dents represented as 180 degree volume angle indentation and 60 degree indentation. The mathematical schemes are shown in Fig. 14. The usage of plate specimen to approximate a 12" standard pipe has been proven valid [11]. Around 1000 elements are used to mesh the boundary of the specimen with the dent defect. The calculated reflection and transmission coefficients are shown in Fig. 15 to Fig. 18.

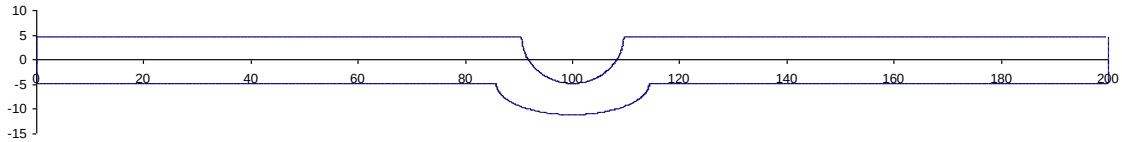

(a) 0.75" diameter, 0.375" depth half-sphere "cup" dent

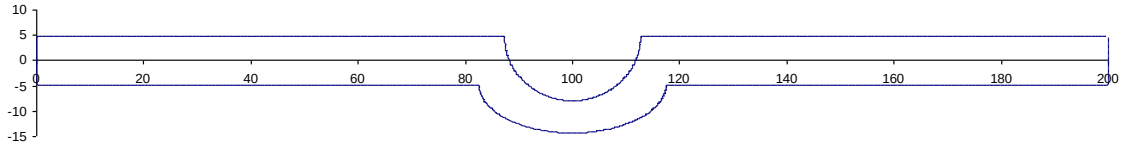

(b) 1" diameter, 0.5" depth half-sphere "cup" dent

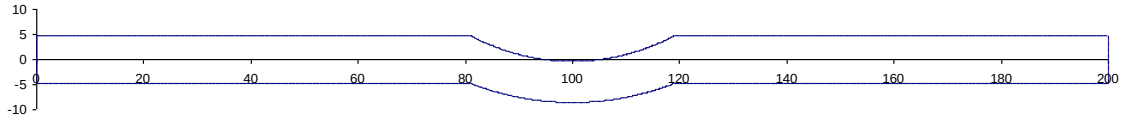

(c) 1.5" diameter, 0.23" depth 60-degree-volume-angle-sphere "saucer" dent

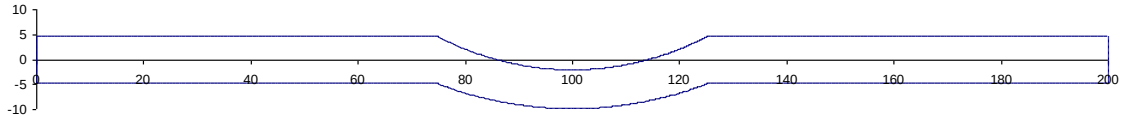

(d) 2" diameter, 0.31" depth 60-degree-volume-angle-sphere "saucer" dent

Fig. 14 BEM model of the "cup" and "saucer" dents

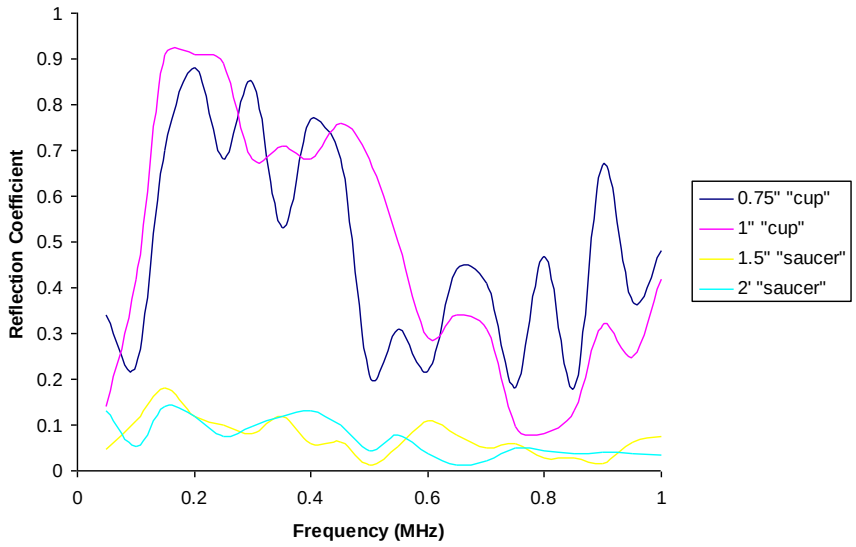

Fig. 15 Reflection coefficient of SH n0 mode wave incident into the dents

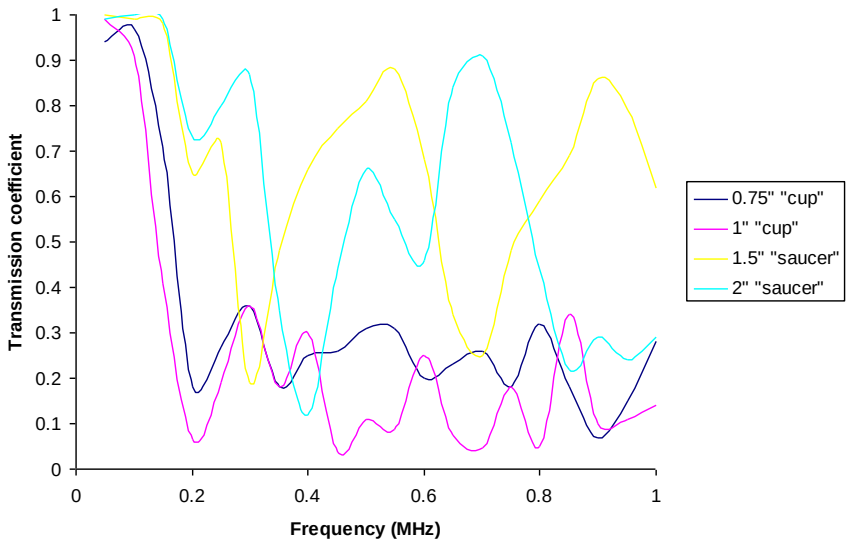

Fig. 16 Transmission coefficient of the SH n0 mode incident into the dents

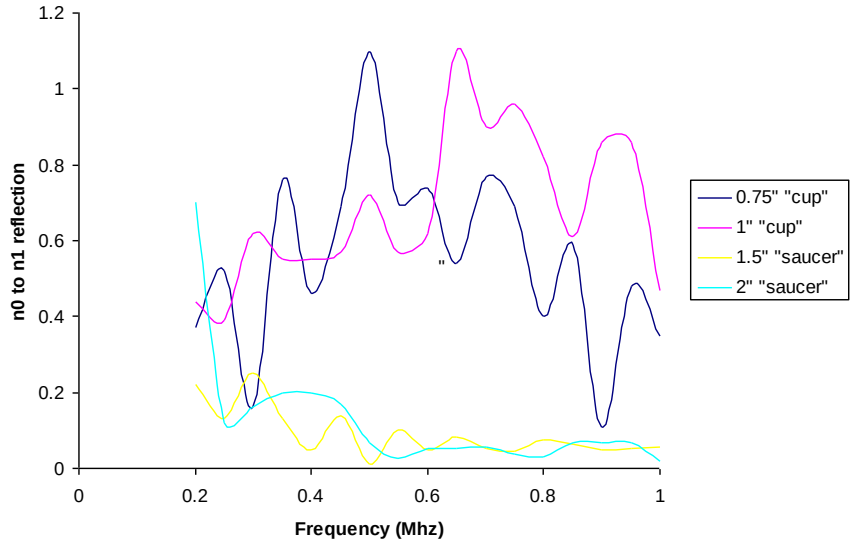

Fig. 17 Reflection coefficient of the mode converted n1 mode for n0 mode SH wave incident into the dents.

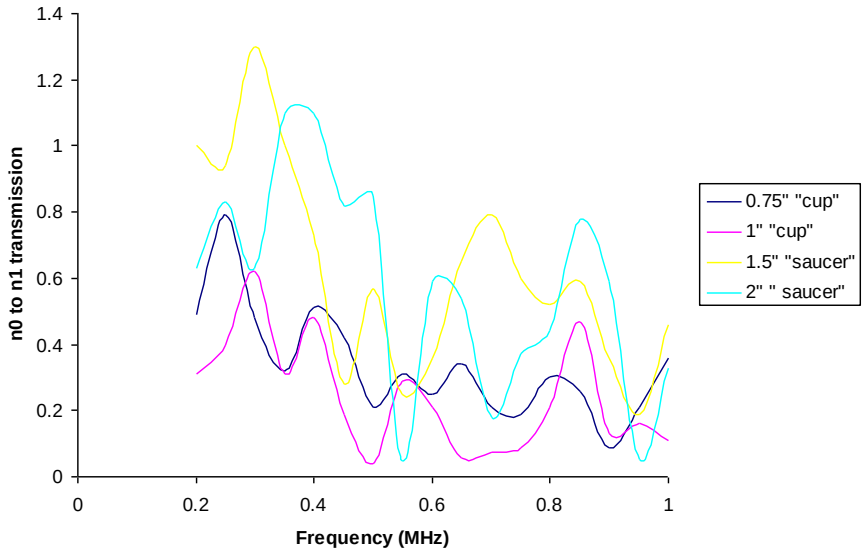

Fig. 18 Transmission coefficient of the mode converted n1 mode for n0 mode SH wave incident into the dents

From the BEM calculation, it is evident that the dent will cause wave reflection and transmission energy partition. Moreover, mode conversion occurs at the defect. n0 mode SH wave incidence will not only result in n0 mode reflection and transmission, but also n1, n2, or even higher mode to appear and energy partition. This feature, though complex, could benefit for the defect classification and sizing since different dents will cause different response of these effects.

It is also seen that the reflection coefficient of the n0 mode SH wave at low frequency region (200 kHz ~ 400 kHz) has distinct response to “cup” dents and “saucer” dents, i.e. high reflection occurs for “cup” dents and much less reflection occurs for “saucer” dents. This could be used for classification purpose. Also, with different size dent, the reflection and transmission coefficient has different values, which could be extracted for defect sizing.

3.2 Defect Classification for man-made notch defects

Oak Ridge Lab. has some EMAT data for man-made notch defects on a 12 inch pipe. In this section, we initiated the effort of developing the defect classification algorithm. SID (Spectrum Information Divergence) similarity measure [12], Orthogonal Subspace Projection (OSP) [12], Nonnegatively Constrained Least Squares (NCLS) [12], and Principal Component Analysis combined with Discriminant Analysis (PCA-DA) [10] were evaluated. Results show that PCA-DA approach has a relatively superior performance over the other methods for EMAT data on a pipe.

3.2.1 Data specification

The experimental data set consists of 300 samples collected from acoustic sensor located on a pipe. The EMATS are 3.375" in dimension (circumferentially), with the active area being 1.35" (circumferential) by 1.5" (width). The distance between the transmitter and receiver EMATs is 1.5". The EMATs were positioned in the center of the defects. Each sample is a time domain data vector, which consists of 2048 data points. The data set has been divided into two sets:

- Training data set, (50 normal, 25 defect1, 25 defect2, 25 defect3, 25 defect4),
- Testing data set (50 normal, 25 defect1, 25 defect2, 25 defect3, 25 defect4).

The types of defects introduced on the pipe and the normal condition are given as:

- Normal: width: none, depth: none,
- Defect1: width: 0.25, depth: 0.2,
- Defect2: width: 0.25, depth: 0.17,
- Defect3: width: 0.125, depth: 0.224,
- Defect4: width: 0.125, depth: 0.185.

Fig. 19 shows the sample waveform for normal data and defect 1 data.

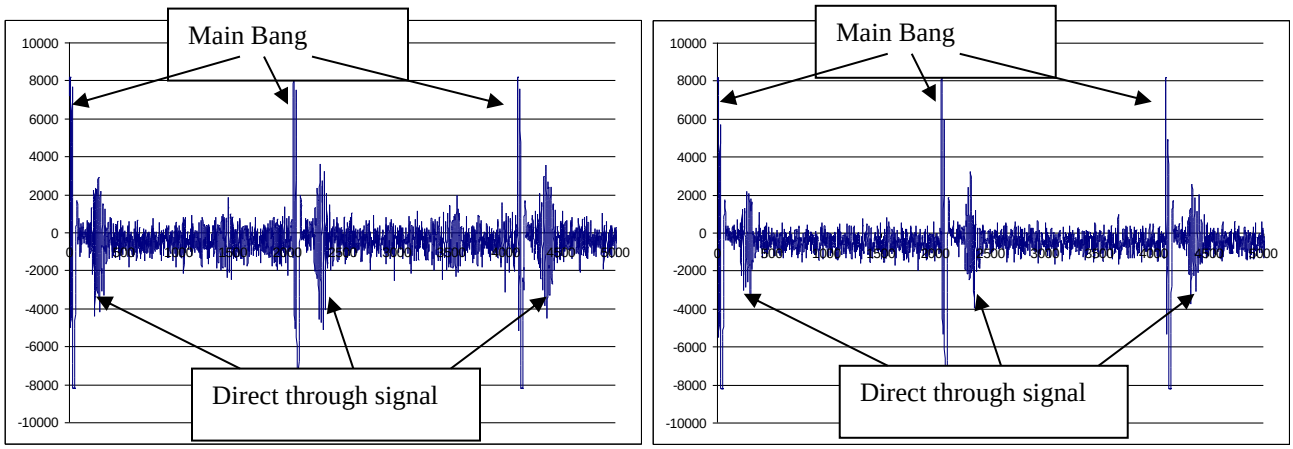

(a) Normal (b) Defect 1

Fig. 19 Collected EMAT transmission waveform of the SH wave incident into notch defects.

3.2.2 Defect Classification Using SID, OSP, NCLS, and PCA-DA

Various methods were used and tested, such as SID (Spectrum Information Divergence) similarity measure, Orthogonal Subspace Projection (OSP), Nonnegatively Constrained Least Squares (NCLS) and Principal Component Analysis combined with Discriminant Analysis (PCA-DA). The details of the algorithms (SID, OSP, NCLS) are shown in the Appendices.

We will not elaborate the details of each method here, but just show one method for illustration purpose. The PCA-DA algorithm is composed of three parts: feature extraction by PSD (Power Spectral Density), feature dimension

reduction by Principal Component Analysis (PCA), and data classification using DA (Discriminant Analysis). The block diagram of the applied classification method is depicted in Fig. 12.

Fig. 13 depicts the PSD of the training and testing data sets between frequencies 80 and 170 (frequency in samples).

- The spectral signatures representing the five different condition of the pipe are obtained by averaging the PSD waveforms of the corresponding training data sets. Fig. 20 depicts the spectral signatures of the five conditions after the averaging process.

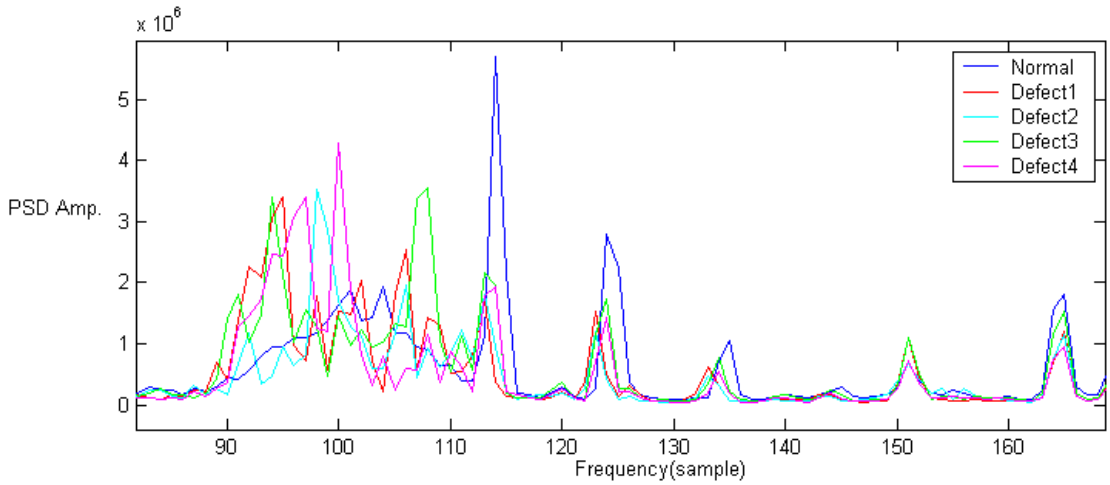

Fig. 20 Spectral signatures of the five pipe conditions after averaging the corresponding PSD waveforms.

To apply the various methods to the EMAT data, the training and testing data sets are randomly separated. Random selection is applied using Matlab's random generator function (rand). Only training data set is used in finding PC eigenvectors. Table 2 gives the evaluation results for these methods. For PCA-DA method, 6, 8, 11 and 14 principal components were evaluated for feature extraction, the PCA Modeling Error Rate definition (MER, see Section 2.2 for definition) for each case were shown in Fig. 21.

Fig. 22 illustrates the results in Table 2 in graphical manner. It can be clearly seen that PCA-DA yielded the best performance. If we choose 8 principal components, we can get close to 100% correct classification accuracy for most of the cases. We also observed that more and less principal components do not yield good performance because of over-training and under-training issues.

Table 2 Results for the testing data on a 12" pipe

	Correct Classification Percentage for Testing Data Sets				
Method	**Healthy**	**Defect1**	**Defect2**	**Defect3**	**Defect4**
SID	98%	100%	100%	88%	88%
OSP	94%	100%	100%	72%	76%
NCLS	94%	96%	100%	72%	80%
PCA-DA (6 PC features)	98%	88%	88%	96%	88%
PCA-DA (8 PC features)	100%	100%	100%	100%	96%
PCA-DA (11 PC features)	100%	92%	100%	100%	96%
PCA-DA (14 PC features)	100%	84%	100%	100%	100%

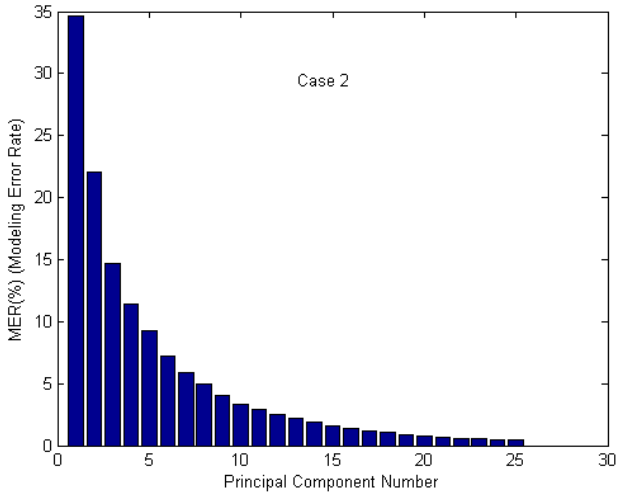

Fig. 21 Modeling error rate (%) with PCA modeling (12" data)

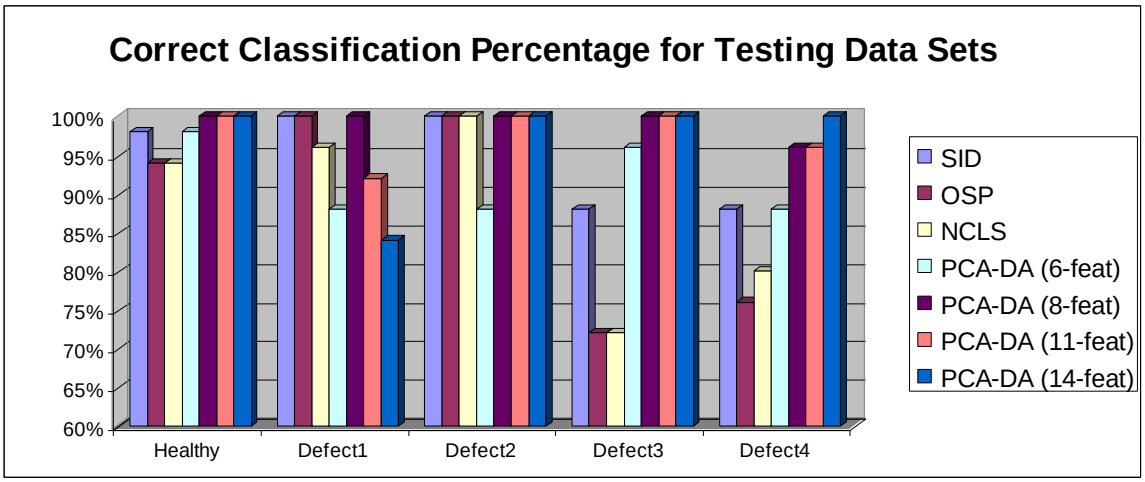

Fig. 22 Classification results of different methods for different defect conditions.

3.3 "Cup" and "Saucer" Defect Detection, Classification, and Size Estimation for 12" Pipe

First, we have successfully fabricated a test specimen with a 7 feet long, 12 inch diameter seamless pipe. Six "cup" dents and ten "saucer" dents were successfully introduced on the outside pipe wall. The dents size, depth and the surrounded area of deformation were measured and cataloged for the rest of the studies.

Second, we set up the SH EMAT data acquisition system and collected a large number of through-transmission data inside the pipe. The data consists of 9 groups of normal data which were collected at 9 different locations in the pipe where there is no visual defect; 30 groups of "cup" dents data, with every five of them were collected through the same "cup" dent but at a slightly different lateral position; and 50 groups of "Saucer" dents, also with every five groups on the same dent.

Third, after the EMAT data were collected for the dents defect, we applied the PCA-DA algorithm to the "cup" and "Saucer" dents as compared to the normal conditions. We can successfully detect any dents of depth larger than 0.1" with 100% correct rate and classify the "cup" dents 100%. This depth is much less than that required by the OPS pipeline safety regulation (0.5" for 12" seamless pipe) [13] and should give maintenance personnel enough confidence margin for critical dents detection. For "Saucer" dents, the correct classification rate is about 70% since the saucer dents we used in the study is less than 0.15". We should be able to achieve 100% correct rate for the deeper dents.

Finally, the dents depths are plotted versus the EMAT through-transmission signals amplitude, which show the reduction in amplitude for increased dent depth and size. The initial linear curve fitting combined with the dent classification algorithm could roughly provide the dent depth information.

In the following sections, technical details of the work performed and the results are presented. Future work plans and financial status are also attached.

3.3.1 Mechanical dents creation and descriptions

Mechanical damage in natural gas pipelines is of great concern to the industry. There is potential for a catastrophic failure if these damages are not detected. Most of these flaws are caused by third party damages during digging around the area where pipelines are buried.

A 12-inch diameter schedule 40 (wall thickness 0.375 inch) seamless steel pipe sample was selected to study the feasibility of detecting these defects using EMATs. In simulating dents, the dents were classified into cups and saucers. The differentiation of a cup and a saucer is based on the severity of the slope of the defect.

Dent Creation

Dents on the pipes were created using a hydraulic press. Chrome finish steel balls of 5-inch, 3.75-inch, 1-inch and 0.75-inch diameter were used for the creation of dents. The pipe was placed on the hydraulic press with support braces under it. A fixture attached to the ram on the hydraulic press secured the steel balls. By controlling the amount of displacement of the ram, the dents of different depth were created. The larger diameter balls were used to create saucer while the smaller ones produced the cups. Fig. 23 shows the diagram of the pipe specimen with the mechanical dents created.

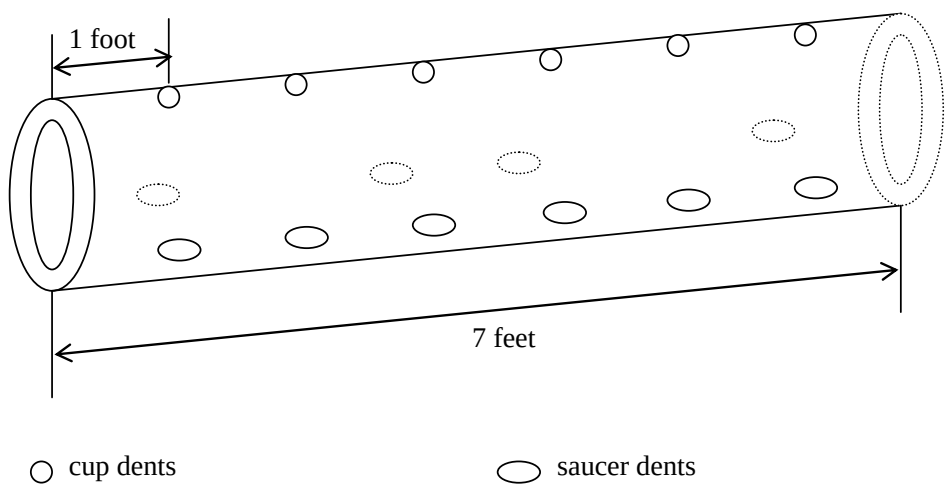

Fig. 23 Three rows of cup and saucer dents created on a 7 feet long, 12 inch diameter schedule 40 seamless pipe. They are 1 foot apart from each other or the pipe end for the same row.

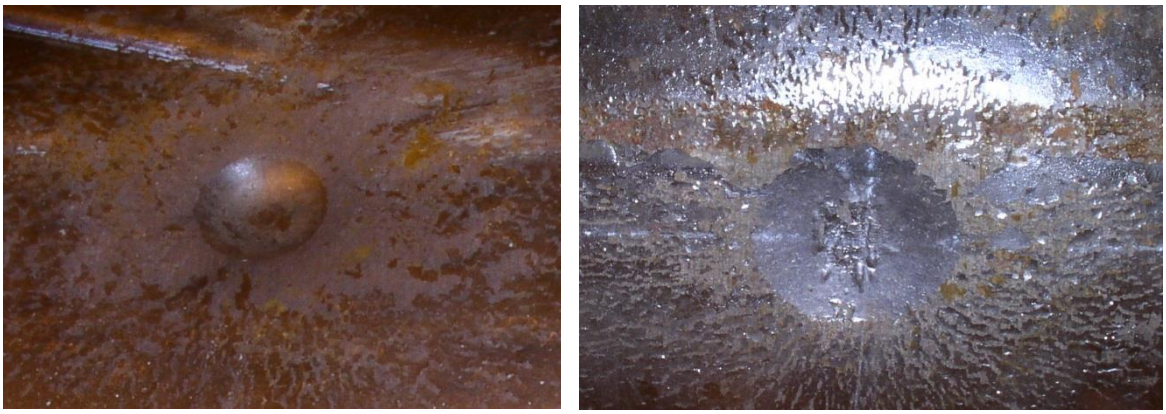

(a) “cup” dent (b) “saucer” dent

Fig. 24 Cup and saucer dents on a 12-inch pipe created by a 0.75” and 5” diameter steel ball

Fig. 24 gives an example of the cup and saucer created on the 12-inch diameter pipe. It can be seen that the cup dent is relatively smaller in size but much sharper, while the saucer dent is flat and large in area. There are also some minor deformations around the dents seen from the photo.

Fig. 25 shows more pictures of the dents created on the 12” schedule 40 seamless pipe. The left column is cup dents, the right are saucers. The programmed indentation depth is shown in each figure. Note that due to deformation recovery of the pipe, the actual size and depth of the dents are much different from what is intended.

(a) 1” ball, pushed 0.2” into the pipe

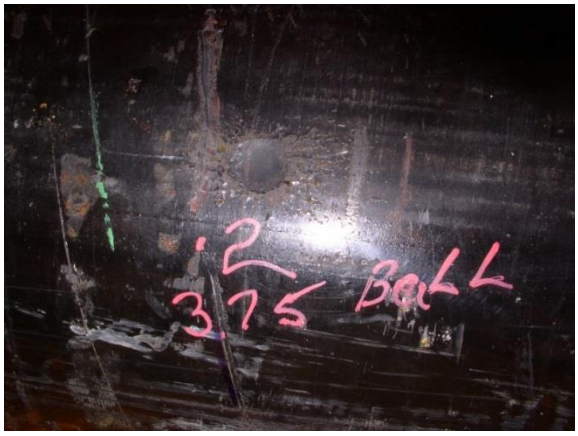

(b) 3.75” ball, 0.2” into the pipe

(c) 0.75” ball, 0.3” into pipe

(d) 5” ball, 0.3” into pipe

(e) 1" ball, 0.375" into pipe

(f) 5" ball, 0.375" into pipe

Fig. 25 Pictures of various cup and saucer dents on a 12" pipe wall

Dent Data

To obtain a representative sample of the EMAT response to varying dent sizes, multiple dents were created. When the steel ball penetrates the 12–inch pipe and creates a dent, the material is displaced, but due to the elasticity of the pipe, the material springs back when the ram is released. The amount of spring back is difficult to predict and control. The depth of the dent created is dependent on how the pipe is secured and where the supports are relative to the ram. In some cases while the ram was pushing the ball into the pipe, the opposite end of the pipe lifted upward. To eliminate all these variables, measurements are based on the dent depth after they have been created and not during the creation of dent. The depths were referenced with the original no-dent condition, i.e., the deepest point of the dent to the original pipe surface.

Table 3 gives values for the depth and area of the dents. Although the ball was spherical, due to the curvature of the pipe circumference, the dents created were ellipsoidal. Table 3 gives the major and minor diameters of the dents. Also, around the area of the dent, there was a region that experienced a flattening or gradual slope to the actual depression of the cup and saucer. This area is referred to as the area of deformation. At the area of deformation, the curvature of the pipe is absent. Fig. 26 explains the shape around the dents.

Table 3 Dent number and size information

Dent Number	Diameter		Depth	Area of deformation	Ball Diameter
	Axial	Circumferential			
1	0.395	0.378	0.085	0.63 x 0.55	0.75
2	0.5	0.488	0.218	1.4 x 0.75	
3	0.444	0.435	0.124	0.95 x0.75	
4	0.415	0.415	0.065	0.625 x 0.625	1
5	0.545	0.534	0.20	1.35 x1.2	
6	0.386	0.375	0.062	0.55 x 0.51	
7	0.72	0.65	0.033	1.25 x 0.875	3.75
8	1.35	0.995	0.118	3 x 3	
9	0.595	0.526	0.04	1.25 x 0.95	
10	1.46	0.855	0.134	2.4 x 1.56	5
11	1.46	0.894	0.121	1.6 x 1.3	
12	0.73	0.715	0.094	1.1 x 1.1	
13	0.615	0.547	0.070	0.95 x 0.65	3.75
14	0.875	0.775	0.179	1.75 x 1.3	3.75
15	0.886	0.75	0.123	1.5 x 1	5
16	0.745	0.62	0.076	1.1 x 0.85	5

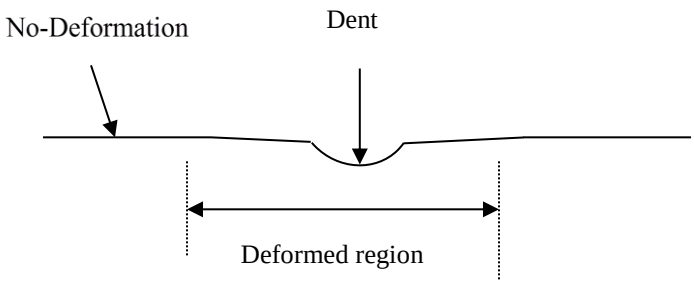

Fig. 26 Diagram of the dent and the induced deformation

3.3.2 EMAT data collection inside the 12-inch pipe

Data collection

After the dents were created on the pipe, EMATs in through-transmission mode were used to collect the data. Fig. 27 shows the pipe specimen and the receiver and transmitter EMAT setup inside the 12-inch pipe.

(a) The 12-inch standard seamless pipe specimen with the dents on the outer surface of the pipe wall

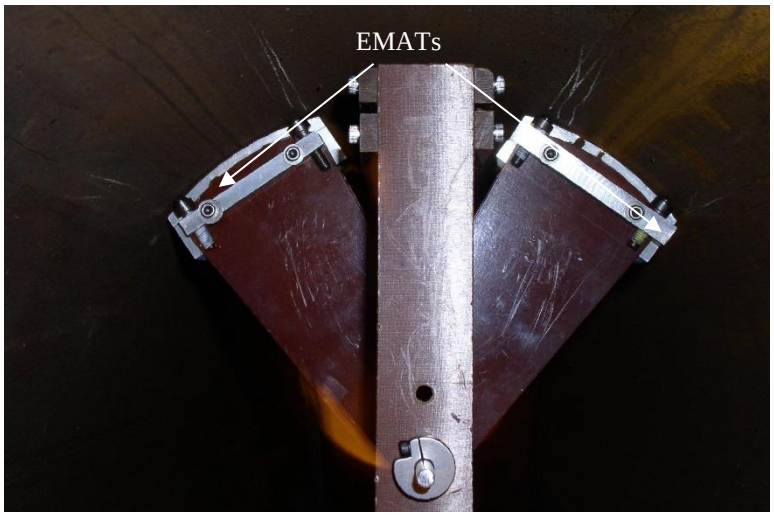

(b) EMAT configured inside the test pipe

Fig. 27 EMAT data collection setup

The flaws were positioned between the two EMATs to obtain the data. The spacing between the transmitter and receiver could be adjusted in the fixture for the particular measurement of interest. For all these tests, the center-to-center transmitter-receiver spacing was set at 6.5- inches. The frequency of the pulser was set at 263.4 KHz with a pulse width of 22 microseconds and a repetition rate of 12 milliseconds. The signals are amplified by 93 dB before being collected by the data acquisition unit.

The EMATs were positioned on either side of the dents while the measurements were taken. For these sets of data, the signals were obtained while the EMATs were stationary. Five measurements were taken for each dent with two readings on either side of the mid-point of the dent and one with the EMAT mid-point coinciding with the dent center. After the successful demonstration of the technology, when the system is field deployed, the measurements have to be obtained while the EMAT are in motion relative to the flaw
Since EMAT measurement in this configuration is not an absolute measurement of the dent, baseline readings were obtained to reference the signal deviation from the norm. To obtain the baseline readings, the EMATs were positioned on the pipe with no visible flaws. Multiple measurements were taken to obtain a good sample of the no-flaw signal.

Fig. 28, Fig. 29, and Fig. 30 show the sample though transmission waveforms for normal, a cup dent and a saucer dent pipe section collected by the EMAT sensors. It is seen that the amplitude of the direct through signal for the cup and saucer dents were reduced. Moreover, the signal from the saucer dent becomes dispersed due to a multi-path effect around the dent, which is less so for the cup dents because of the smaller size.

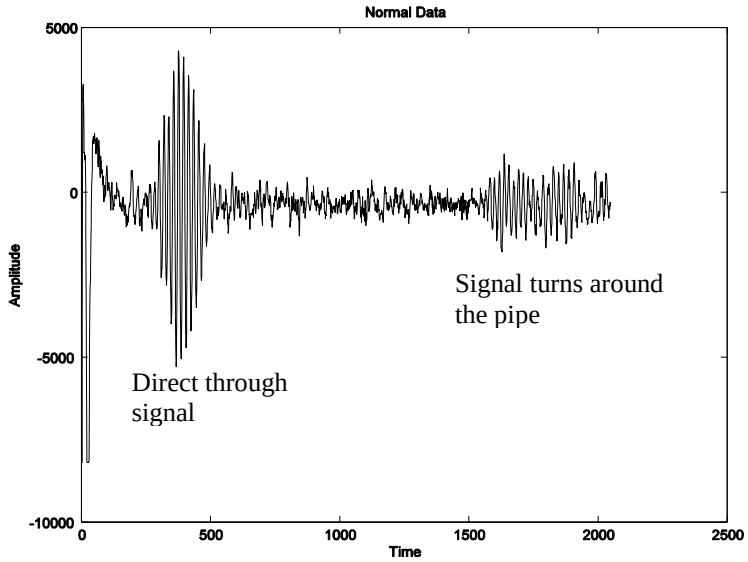

Fig. 28 Data Scan of normal position

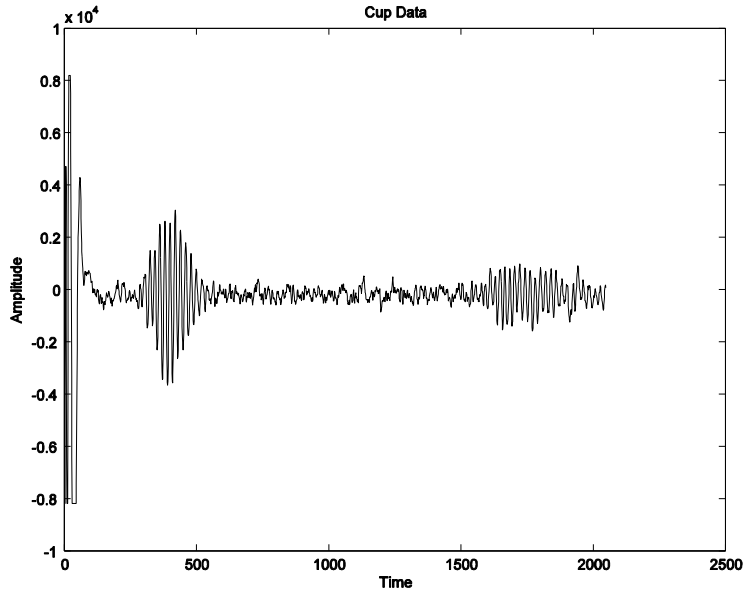

Fig. 29 Data scan of Cup type defect

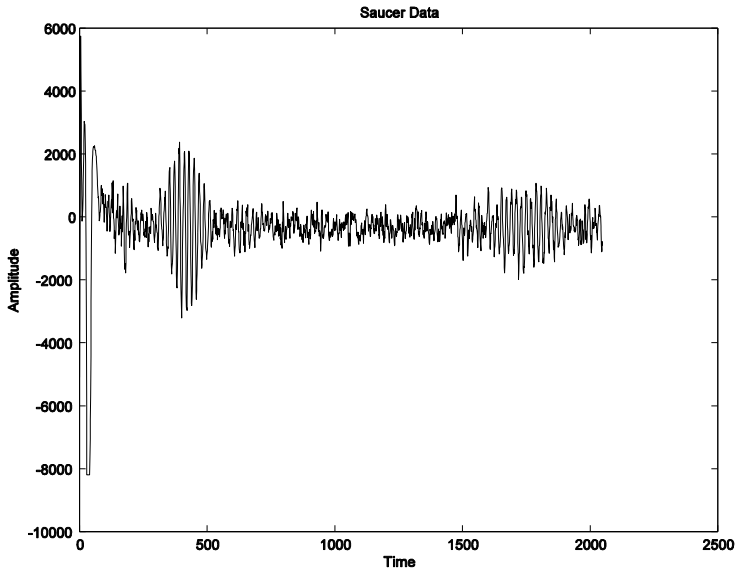

Fig. 30 Data scan of Saucer type defect

3.3.3 Defect Detection Based on Correlation Technique

We noticed that for shallow dents (i.e., depth less than 0.1 inch), the waveform did not show much visual difference from the normal data, which is understandable since the defect is too small and not much change were made to the through transmission waveform. Our initial classification algorithm also did not perform well. This could be viewed as a detection limitation of EMAT for the dents detection in the pipelines.

Here we apply a time domain cross-correlation method to the dents data (for depth larger than 0.1 inch) collected by EMAT sensors. We selected 90 samples of normal data, 150 samples of cup data, and 150 samples of saucer data for dents detection and classification. The dents are all have depth larger than 0.1 inch. Note that for each position 10 samples will be collected. Thus we only need to do the classification for every 10 samples.

The objective is to first determine if there is a defect for each new position. If there is, we need to do the classification between Cup and Saucer types of defect. Therefore, we can use time domain correlation of main lobes to determine if there is a defect or not. The correlation value is calculated by the following procedures:

(1) Use the first normal scan as the reference sample.
(2) For any new sample, first shift it in the time domain so that the correlation value $\sum_{i \in Mainlobe} \mathrm{Re}\, f_i \bullet NewSample_i$ is maximized.
(3) The outcome correlation value is the correlation value of this new sample to reference sample.

The correlation values of all 390 samples are shown in Fig. 31. Here first 90 samples are normal data, and all the other samples are defect data.

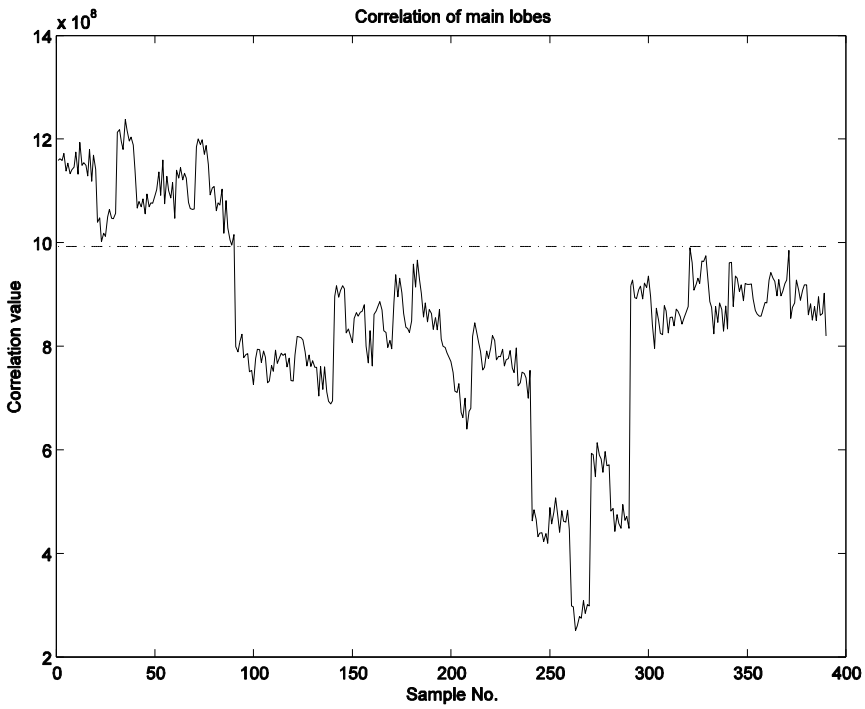

Fig. 31 Cross-Correlation value of all samples

As we can see, by choosing an appropriate threshold, we can determine if there is a defect or not. Using the data we have and choosing the threshold shown by the dotted line in Fig. 31, the dents are successfully detected without any error. Table 4 summarizes the detection results.

Table 4 Results for the testing data sets regarding the Normal/Defect classification.

	Number of samples	Labeled as Normal	Labeled as Defect	Accuracy
Normal	80	80	0	100%
Defect	300	0	300	100%

3.3.4 PCA based Technique for Classification

After we determine there is a defect in the specified position, we need to classify the defect as Cup or Saucer. Time domain correlation methods are no longer enough in this case. Instead, we will use PCA-DA based classification. The data set has been divided into two sets:

- Training data set, (100 Cup, 100 Saucer),
- Testing data set (50 Cup, 50 Saucer).

A total of 14 principal component features have been used, and the test results are shown in Table 5.

Table 5 Results for the testing data sets regarding the Cup/Saucer classification.

	Number of samples	Labeled as Cup	Labeled as Saucer	Accuracy
Cup	50	50	0	100%
Saucer	50	17	33	66%

We can see that with the PCA-DA algorithm, we can successfully detect cup dents deeper than 0.1 inch with no error. This is critical since cup dents are considered more harmful to the safety of the transmission lines. The classification rate for saucer dents is not as good as cup dents, however, with more EMAT data and more dents specimen, we could produce a table or a PD/FLR curve for each type of dents so that the inspection personnel have a better picture of how effective the EMAT PIG and what the inspection limitation is.

To help users further visualize the classification results, we plotted the first three principal features (Fig. 32). It can be seen that there are some overlapping because we only used 3 out of 14 features. However, the 3-D indeed provides an easy and straightforward way for users to visualize the differences between cup and saucer defects.

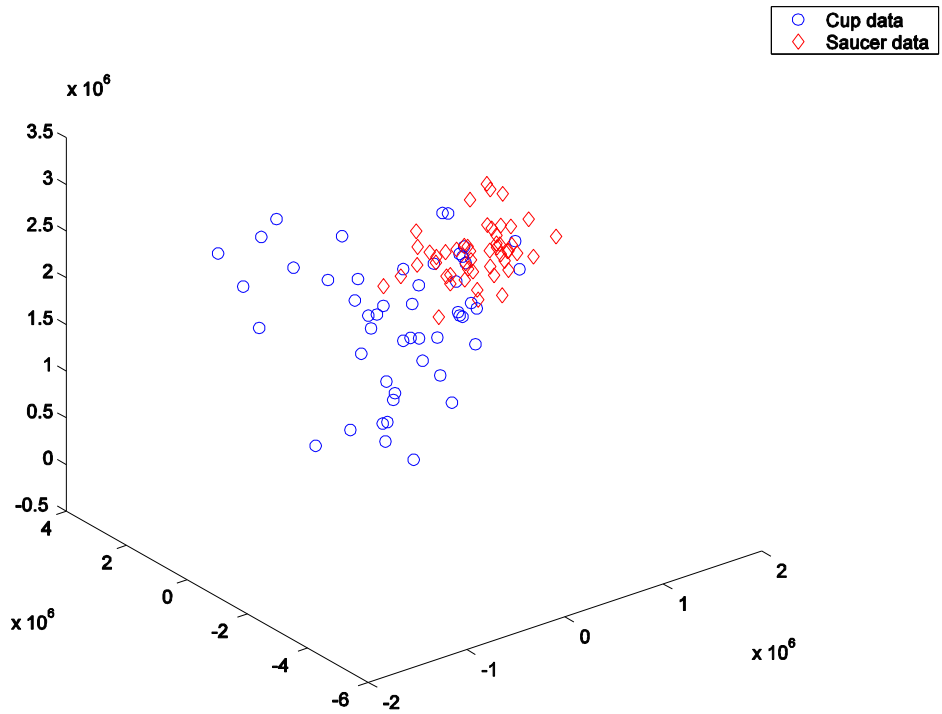

Fig. 32 PCA features of old defected data

3.3.5 Dent depth Estimation

Since we know the signal amplitude information of a newly collected signal and the normal reference signal, upon successfully separating the “cup” and “saucer” dents, we can use the waveform envelop to approximately estimate the depth of the dents. This will certainly provide some useful information for the pipeline inspector.

Here we tried to examine how the dent depths correlate to the EMAT through-transmission signal. All the 9 groups of normal data, 6 groups of cup data and 10 groups of saucer data were calculated for their signal envelop. The peak value of the direct through signal envelop were then plotted versus the dent depth. The results are shown in Fig. 33. Note that for each dent, 10 frames of data at the center position were used, and their peak values of the direct signal are plotted in the figure. Due to the presence of background noise, the peak amplitudes of the signals have some variances, resulting in clusters in the figure. Two dashed lines were drawn in the figure to roughly fit the trend of the clusters, showing that the overall amplitudes of both the cup and saucer dents decrease with the increase of dent depth. However, there are some local amplitude variances due to the constructive and destructive interferences of SH wave passing through different sizes of dents and the EMAT data collection conditions. The saucer dents amplitude decreases more for the same depth compared to the cup dents, which complies with our intuition since saucers have larger dented area and block more wave energy that is coming through.

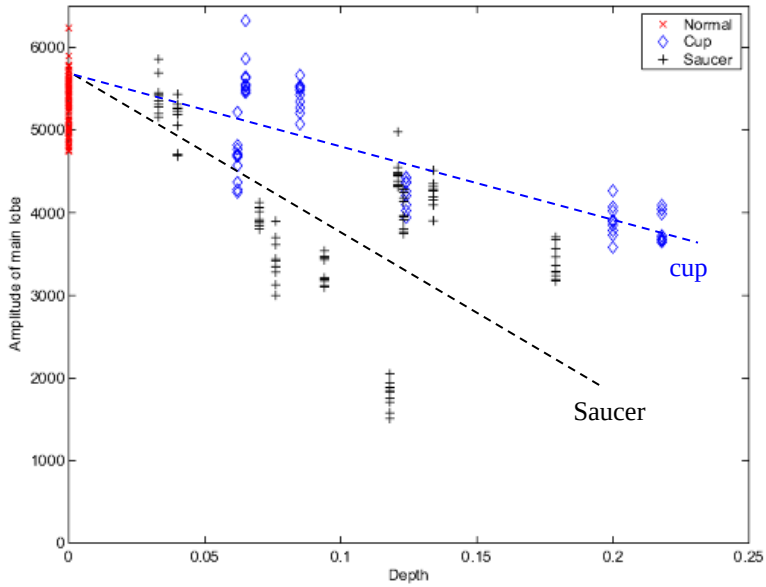

Fig. 33 EMAT through-transmission signal amplitude versus the dent depth showing the overall decreasing signal strength with deeper dents. Saucer dents experienced a relatively sharper decrease compared to the cups. This information can be used inversely to estimated the dent depth after "cup" and "saucer" separation

3.4 Defect Detection and Classification for another 12" Pipe

In Section 3.3, we presented results of defect detection for a 12" pipe. After that, we also created many new dents on a new 12" pipe. Here we briefly summarize the latest results in this section.

Our approach consists of two steps. First, we applied correlation analysis to determine whether a given measurement is normal or defective. Second, we applied PCA-DA to further classify the defect type.

The correlation values of all 600 samples are shown in Fig. 34. Here first 100 samples are normal data, and all the other samples contain defects.

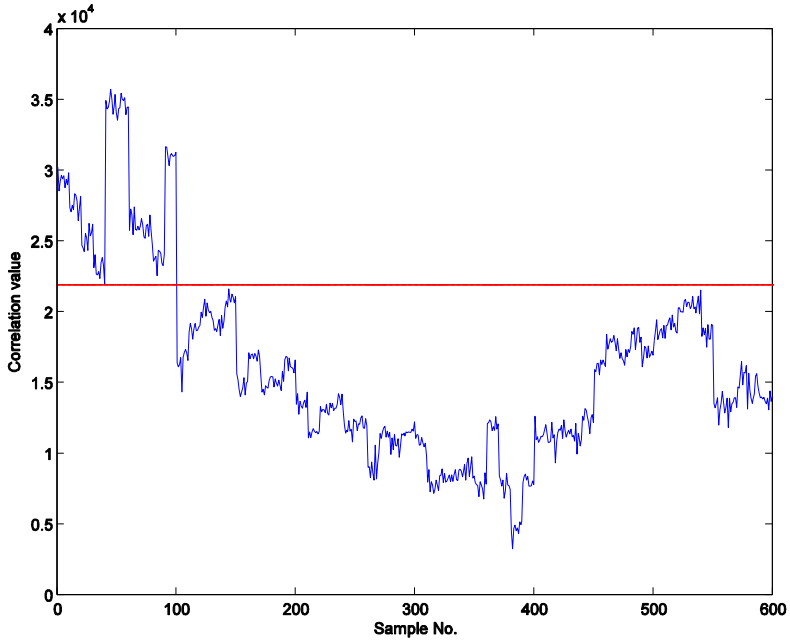

Fig. 34: Correlation value of all samples from new data set

As we can see, if we choose an appropriate threshold, we can determine if there is a defect or not. Using the data we have and choosing the threshold shown by the dotted line in Fig. 34, the probability of error is 0. Table 6 shows the results.

Table 6. Results for the testing data sets regarding the Normal/Defect classification.

	Number of samples	Labeled as Normal	Labeled as Defect	Accuracy
Normal	90	90	0	100%
Defect	500	0	500	100%

After we determine there is a defect in the specified position, we need to classify the defect as Cup or Saucer. Time domain correlation methods are no longer enough in this case. Instead, we will use PCA-DA based classification. The data set has been divided into two sets:

- Training data set, (250 Cup, 150 Saucer),
- Testing data set (50 Cup, 50 Saucer).

A total of 14 principal component features have been used, and the results are shown in Table 7.

Table 7 Results for the testing data sets regarding the Cup/Saucer classification.

	Number of samples	Labeled as Cup	Labeled as Saucer	Accuracy
Cup	50	48	2	96%
Saucer	50	15	35	70%

To help users visualize the defect classification results, we plotted the first 3 principal features in a feature space as shown in
Fig. 35. Since we used only the first 3 PCA features of these test data, there are some overlappings. However, most of the data sets are separable.

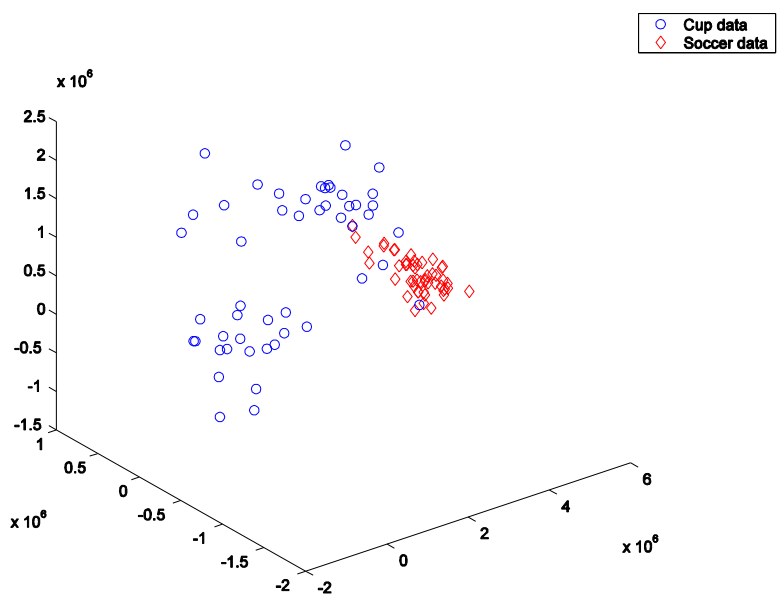

Fig. 35: PCA features of defect data.

3.5 Graphical User Interface for Demonstrations

To help people understand the performance of our algorithms, we developed a Graphical User Interface (GUI). The processed results have been saved into files. Our GUI can display raw data and the processed data. We can compare the ground truth with the detection and classification results. Fig. 36 shows the GUI. Although our system is not running in real-time yet, the GUI will be the same for the real-time version.

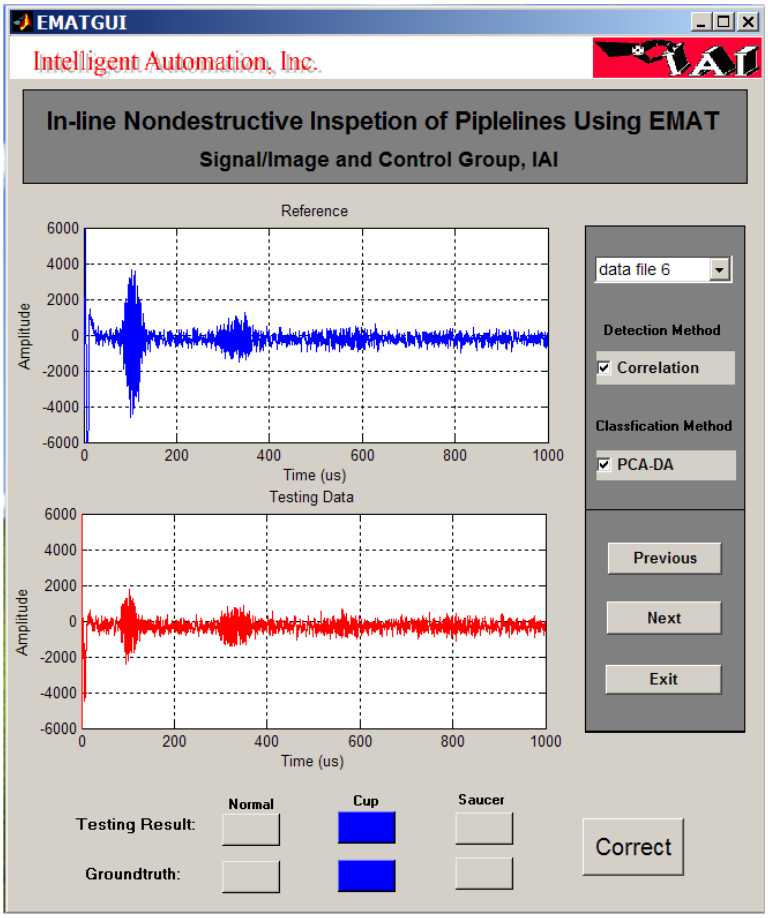

Fig. 36 GUI for pipeline defect detection and classification.

4. Conclusions

In this Phase 1 research, we have clearly demonstrated the proposed approach for detecting and classifying "cup" and "saucer" dents in pipes. Extensive simulations and comparative studies were performed. Specifically, we have observed that:

- EMAT transducers are quite sensitive in detecting small dents (0.1"), which are much less that the minimum dent size (0.25") required for safety by the pipeline inspection community.
- Extensive experiments were performed to create dents with different sizes.
- Correlation analysis was used for defect detection. The performance was perfect.
- Four defect classification algorithms were implemented and evaluated. The PCA-DA was selected as a candidate for Phase 2 implementation. Our evaluation results showed that we can correctly classify over 95% of cup defects and near 70% of saucer defects.
- Initial theoretical developments based on Boundary Element Method showed that the frequency and mode information will be valuable for further improving the performance of defect detection and classification.

5. Future Work

Phase 2 Work Plan

- Task 1: Further developments in theoretical studies.
  Task 1.1: Arrange a kickoff meeting; further refine the pipeline inspection problem and objective.
  Task 1.2: Further study the guided wave scattering phenomenon from a 3-D perspective so that the detection and classification algorithms have a stronger physics based foundation.
  Task 1.3: Further study the features for dent size estimation, both in area and depth.

- Task 2: Perform experiments on large diameter pipes (between 20" to 40").
  In phase I we focused our effort on the feasibility study of our proposed approach for the pipe dents inspection. The pipe specimens were 12-inch diameter. In phase II, we will extend our techniques to both the transmission line and distribution network.

  Task 2.1: Obtain pipes of diameter larger than 20 inches, produce mechanical dents or other defects on the specimen
  Task 2.2: Custom design EMAT sensors for the specific pipes, take consideration of the wall thickness change and curvatures.
  Task 2.3: Perform data collection and validate our detection and classification algorithms.

- Task 3: Develop PIGs for either the small diameter pipe or large diameter pipe.
  In phase I, our study is still in a static data collection mode, i.e., the EMATs are not moving when collecting data. This will be quite different from collecting data on a moving platform. More noises will be introduced if the EMATs are constantly moving inside the pipe. Also, the pipe thickness variation will play a role in deteriorating the signal quality. We have the experience of developing an EMAT PIG system. A brief description of such a system developed by our subcontractor is shown in the Appendix.

  Task 3.1: Study the effect of a moving EMAT sensor on data collection; suppress inherent noises and variations due to the pipe wall thickness variations.
  Task 3.2: Based on the market needs and DOT engineer input, initiate the design for a PIG system for either the gas transmission line or distribution network.
  Task 3.3: Address the potential problem of pipe curvature change or ovulation, finalize the prototype PIG system

- Task 4: Further improve and optimize the algorithms developed in Phase 1
  Task 4.1: Further improve the dents classification rates.
  Task 4.2: Capability of dent size estimation
  Task 4.1: Capability to deal with noise

Task 4.2: Capability to extract defect signature and deal with new type of defect other than dents

- Task 5: Implement the algorithms in real-time hardware
  Task 5.1: Integrate and test the software together in the MATLAB environment
  Task 5.2: Implement the selected algorithm in the prototype PIG
  Task 5.3: Setup the communications between software and hardware; develop the Graphical User Interface (GUI) for the operator

- Task 6: Perform real-time laboratory tests
  Task 6.1: Debug the PIG system hardware and software, perform the real-time test in the pipe specimen.
  Task 6.2: Evaluate the integrated system

- Task 7: Perform real-time demonstrations at Oak Ridge Lab. and DOT
  Task 7.1: Finalize the hardware and software of the prototype PIG system, package the system for the lab test.
  Task 7.2: Demonstration of the PIG system for real-time mechanical dents and possible other defect detection, classification and size estimation

- Task 8: Commercialization
  Task 8.1: Advertise and demonstrations of the system for industries and other government agencies; attract investments for phase 3 product development.

6. References

[1] I. A. Viktorov, Rayleigh and Lamb Waves (Plenum, New York, 1970).
[2] B. Auld, Acoustic Fields and Waves in Solids (Krieger, Malabar, Florida, 1990).
[3] J. Rose, Ultrasonic Waves in Solid Media (Cambridge University Press, Cambridge, 1999).
[4] X. Zhao and J.L. Rose, "Guided circumferential shear horizontal waves in an isotropic hollow cylinder," *The Journal of the Acoustical Society* of America, Vol.115, 1912-1916, 2004.
[5] C. Brebbia, J. Tells and L. Wrobel, Boundary Element Techniques (Springer, Berlin,1984).
[6] J. Dominguez, Boundary Elements in Dynamics, (Computational Mechanics Publications, Southampton, Boston, 1993).
[7] J.L. Rose, P. Karpur and V. Newhouse, "Utility of Split-spectrum processing in ultrasonic nondestructive evaluation" *material evaluation*, Vol. 46, 114-122, 1988.
[8] X. Zhao, J. L. Rose, "Boundary Element Modeling for defect characterization potential in a wave guide", *International Journal of Solids Structures*, Vol. 40, 2645-2658, 2003.
[9] X. Zhao, J.L. Rose, "Three Dimensional Boundary Element Modeling for Guided Waves Scattering from a Defect," *Review of Progress in Quantitative NDE*, Vol. 23, 132-138, 2004.
[10] S. Haykin, *Neural Networks*, Prentice Hall, 1990.
[11] X. Zhao, J. L. Rose, "Guided circumferential shear horizontal waves in an isotropic hollow cylinder," *J. Acoust. Soc. Am.*, Vol. 115, 1912-1916, 2004.
[12] C. Chang, *Hyperspectral Imaging: Techniques for Spectral Detection and Classification*, Kluwer Academic/Plenum Publishers, 2003
[13] DOT 49 CFR Part 192[Docket No. RSPA–00–7666; Notice 4] RIN 2137–AD54 Pipeline Safety: Pipeline Integrity Management in High Consequence Areas (Gas Transmission Pipelines)

7. Appendices

7.1 Spectral Information Divergence (SID) [12]

Assume that $\mathbf{s}_i = (s_{i1}, s_{i2}, \cdots, s_{iL})^T$ and $\mathbf{s}_j = (s_{j1}, s_{j2}, \cdots, s_{jL})^T$ are two spectral signatures. Let $\mathbf{p} = (p_1, p_2, \cdots, p_L)^T$ and $\mathbf{q} = (q_1, q_2, \cdots, q_L)^T$ the two probability mass functions generated by $\mathbf{s}_i = (s_{i1}, s_{i2}, \cdots, s_{iL})^T$ and $\mathbf{s}_j = (s_{j1}, s_{j2}, \cdots, s_{jL})^T$ respectively with $p_l = s_{il} / \sum_{l=1}^{L} s_{il}$ and $q_l = s_{jl} / \sum_{l=1}^{L} s_{jl}$. So, the self-information provided by $\mathbf{s}_i$ and $\mathbf{s}_j$ for band l is defined by

$$I_l(\mathbf{s}_i) = -\log p_l \,. \tag{1}$$

$$I_l(\mathbf{s}_j) = -\log q_l \tag{2}$$

respectively. By virtue of Eqs. (1-2) we can define the discrepancy of the self-information of band image B_l provided by $\mathbf{s}_j$ relative to the self-information of band image B_l provided by $\mathbf{s}_i$, denoted by $D_l(\mathbf{s}_i \,\|\, \mathbf{s}_j)$ as

$$D_l(\mathbf{s}_i \,\|\, \mathbf{s}_j) = I_l(\mathbf{s}_i) - I_l(\mathbf{s}_j) = \log(p_l / q_l) \,. \tag{3}$$

Averaging $D_l(\mathbf{s}_i \,\|\, \mathbf{s}_j)$ in Eq. (3) over all the band images $\{B_l\}_{l=1}^{L}$ results in

$$D(\mathbf{s}_i \,\|\, \mathbf{s}_j) = \sum_{l=1}^{L} D_l(\mathbf{s}_i \,\|\, \mathbf{s}_j) p_l = \sum_{l=1}^{L} p_l \log(p_l / q_l) \tag{4}$$

where $D(\mathbf{s}_i \,\|\, \mathbf{s}_j)$ is the average discrepancy in the self-information of $\mathbf{s}_j$ relative to the self-information of $\mathbf{s}_i$. In the context of information theory, $D(\mathbf{s}_i \,\|\, \mathbf{s}_j)$ in Eq. (4) is called the relative entropy of $\mathbf{s}_j$ with respect to $\mathbf{s}_i$ which is also known as Kullback-Leibler information measure, directed divergence or cross entropy. Similarly, we can also define the average discrepancy in the self-information of $\mathbf{s}_i$ relative to the self-information of $\mathbf{s}_j$ by

$$D(\mathbf{s}_j \,\|\, \mathbf{s}_j) = \sum_{l=1}^{L} D_l(\mathbf{s}_j \,\|\, \mathbf{s}_i) q_l = \sum_{l=1}^{L} q_l \log(q_l / p_l) \,. \tag{5}$$

Summing Eqs. (5) and (6) yields Spectral Information Divergence (SID) defined by

$$\mathrm{SID}(\mathbf{s}_i, \mathbf{s}_j) = D(\mathbf{s}_i \,\|\, \mathbf{s}_j) + D(\mathbf{s}_j \,\|\, \mathbf{s}_i) \,, \tag{6}$$

which can be used to measure the discrepancy between two pixel vectors $\mathbf{s}_i$ and $\mathbf{s}_j$ in terms of their corresponding probability mass functions, $\mathbf{p}$ and $\mathbf{q}$. It should be noted that while $\mathrm{SID}(\mathbf{s}_i, \mathbf{s}_j)$ is symmetric, $D(\mathbf{s}_i \,\|\, \mathbf{s}_j)$ is not. This is because $\mathrm{SID}(\mathbf{s}_i, \mathbf{s}_j) = \mathrm{SID}(\mathbf{s}_j, \mathbf{s}_i)$ and $D(\mathbf{s}_i \,\|\, \mathbf{s}_j) \neq D(\mathbf{s}_j \,\|\, \mathbf{s}_i)$.

7.2 Orthogonal Subspace Projection (OSP) [12]

Suppose that there are p targets, $\mathbf{t}_1, \mathbf{t}_2, ..., \mathbf{t}_p$. Let $\mathbf{m}_1, \mathbf{m}_2, ..., \mathbf{m}_p$ be their corresponding spectral signatures. Suppose L is the number of spectral bands in $\mathbf{m}_j$, where $1 \le j \le p$. Let $\mathbf{r}$ denote a linear mixture of $\mathbf{m}_1, \mathbf{m}_2, ..., \mathbf{m}_p$ with appropriate abundance fractions specified by $\alpha_1, \alpha_2, ..., \alpha_p$, which can be denoted by a $L \times 1$ column vector. Let $\mathbf{M}$ denote the $L \times p$ target spectral signature matrix, depicted by $\left[\mathbf{m}_1, \mathbf{m}_2, ..., \mathbf{m}_p\right]$. Let $\boldsymbol{\alpha} = \left[\alpha_1, \alpha_2, ..., \alpha_p\right]^T$ be a $p \times 1$ abundance column vector associated with $\mathbf{r}$, where α_j denotes the abundance fraction of $\mathbf{m}_j$ that is present in the mixture $\mathbf{r}$. The spectral signature of the mixture, $\mathbf{r}$, can be modeled in a linear regression form as follows:

$$\mathbf{r} = \mathbf{M}\boldsymbol{\alpha} + \mathbf{n} \,, \tag{8}$$

where $\mathbf{n}$ is the noise or can be interpreted as a measurement error or a model error.

Further we can rewrite it as

$$\mathbf{r} = \mathbf{d}\alpha_p + \mathbf{U}\gamma + \mathbf{n} \tag{9}$$

where $\mathbf{d} = \mathbf{m}_p$ is denoted as the desired spectral signature $\mathbf{m}_p$ and $\mathbf{U} = [\mathbf{m}_1\ \mathbf{m}_2\ ...\ \mathbf{m}_{p\text{-}1}]$ is the undesired target spectral signature matrix.

An OSP detector denoted by $\delta_{OSP}(\mathbf{r})$ is given by

$$\delta_{OSP}(\mathbf{r}) = \mathbf{d}^{\mathrm{T}} P_U^{\perp} \mathbf{r} \tag{10}$$

where $P_U^{\perp} = \mathbf{I}_{L\times L} - \mathbf{U}\mathbf{U}^{\#} = \mathbf{I}_{L\times L} - \mathbf{U}(\mathbf{U}^{\mathrm{T}}\mathbf{U})^{-1}\mathbf{U}^{\mathrm{T}}$.

Based on OSP, a least-squares estimator, denoted by $\delta_{LS}(\mathbf{r})$ which is referred to as *a posteriori* OSP is given by

$$\hat{\alpha}_p = \delta_{LS}(\mathbf{r}) = (\mathbf{d}^{\mathrm{T}} P_U^{\perp} \mathbf{d})^{-1} \delta_{OSP}(\mathbf{r}) \tag{11}$$

Using Eq. (11), we can estimate the abundance fraction α_p of the desired target signature $\mathbf{m}_p$ in the mixed signature $\mathbf{r}$.

7.3 Nonnegatively Constrained Least Squares Method (NCLS) [12]

The NCLS approach is related to the following optimization problem

$$\text{Minimize LSE} = \left(\mathbf{M}\boldsymbol{\alpha} - \mathbf{r}\right)^T \left(\mathbf{M}\boldsymbol{\alpha} - \mathbf{r}\right) \text{ subject to } \alpha_j \geq 0, \tag{12}$$

where LSE is the least squares error used as a criterion for optimality, and $\alpha_j \geq 0$ represents the nonnegativity constraint for $1 \leq j \leq p$. In order to use the Lagrange multiplier method, a *p*-dimensional unknown positive constraint vector $\mathbf{c} = \left[c_1, c_2, ..., c_p\right]^T$ with $c_j \geq 0$ is introduced, where $1 \leq j \leq p$. A Lagrangian, $J(\boldsymbol{\alpha})$, by means of $\mathbf{c}$ is formed as follows

$$J(\boldsymbol{\alpha}) = (1/2)\left(\mathbf{M}\boldsymbol{\alpha} - \mathbf{r}\right)^T \left(\mathbf{M}\boldsymbol{\alpha} - \mathbf{r}\right) + \boldsymbol{\lambda}^T(\boldsymbol{\alpha} - \mathbf{c}), \tag{13}$$

subject to the constraint $\boldsymbol{\alpha} = \mathbf{c}$. Differentiating $J(\boldsymbol{\alpha})$ with respect to $\boldsymbol{\alpha}$ yields

$$\left.\frac{\partial J(\boldsymbol{\alpha})}{\partial \boldsymbol{\alpha}}\right|_{\hat{\boldsymbol{\alpha}}_{\mathrm{NCLS}}} = 0 = \mathbf{M}^T\mathbf{M}\hat{\boldsymbol{\alpha}}_{\mathrm{NCLS}} - \mathbf{M}^T\mathbf{r} + \boldsymbol{\lambda}. \tag{14}$$

Equation (14) results in the following two iterative equations

$$\hat{\boldsymbol{\alpha}}_{\mathrm{NCLS}} = \left(\mathbf{M}^T\mathbf{M}\right)^{-1}\mathbf{M}^T\mathbf{r} - \left(\mathbf{M}^T\mathbf{M}\right)^{-1}\boldsymbol{\lambda} = \hat{\boldsymbol{\alpha}}_{\mathrm{LS}} - \left(\mathbf{M}^T\mathbf{M}\right)^{-1}\boldsymbol{\lambda}, \tag{15}$$

where $\hat{\boldsymbol{\alpha}}_{\mathrm{LS}}$ depicts the least squares estimate of $\boldsymbol{\alpha}$ and is expressed as

$$\hat{\boldsymbol{\alpha}}_{\mathrm{LS}} = \left(\mathbf{M}^T\mathbf{M}\right)^{-1}\mathbf{M}^T\mathbf{r} \tag{16}$$

Equations (15) and (16) can be used iteratively to solve the optimal solution $\hat{\boldsymbol{\alpha}}_{\mathrm{NCLS}}$ utilizing the Lagrange multiplier vector $\boldsymbol{\lambda} = \left[\lambda_1, \lambda_2, ..., \lambda_p\right]^T$.

In the NCLS algorithm, the components of the estimate $\hat{\boldsymbol{\alpha}}_{\mathrm{LS}}$ is decomposed into two index sets, which are called active set, R, and passive set, *P*, respectively. The active set, *R*, consists of all indices corresponding to negative (or zero) components. The passive set, *P*, contains indices corresponding to positive components in the estimate $\hat{\boldsymbol{\alpha}}_{\mathrm{LS}}$. The algorithm starts with an empty set of *P*, $P = \varnothing$, assuming that the active set contains all components of $\hat{\boldsymbol{\alpha}}_{\mathrm{LS}}$, $R = \{1, 2, ..., p\}$. The sets P and R are then adjusted via iterations using equations (15) and (16). The final generated

passive set depicts the components that are legitimate to be used in the abundance estimation, $\hat{\boldsymbol{\alpha}}_{\mathrm{LS}}$. The NCLS algorithm can be implemented as follows [1]:

1. Initialization: Set the passive set $P^{(k)} = \{1, 2, ..., p\}$, and active set $R^{(0)} = \varnothing$. Set $k = 0$.
2. Compute $\hat{\boldsymbol{\alpha}}_{\mathrm{LS}}$ using (16). Let $\hat{\boldsymbol{\alpha}}_{\mathrm{NCLS}}^{(k)} = \hat{\boldsymbol{\alpha}}_{\mathrm{LS}}$.
3. At the k-th iteration, if all components in $\hat{\boldsymbol{\alpha}}_{\mathrm{NCLS}}^{(k)}$ are positive, the algorithm is terminated; otherwise, continue.
4. Let $k \leftarrow k+1$.
5. Move all indices in $P^{(k-1)}$ that correspond to negative components of $\hat{\boldsymbol{\alpha}}_{\mathrm{NCLS}}^{(k-1)}$ to $R^{(k-1)}$. Let the resulting index sets be denoted by $P^{(k)}$ and $R^{(k)}$, respectively. Create a new index set $S^{(k)}$ and set it equal to $R^{(k)}$.
6. Let $\hat{\boldsymbol{\alpha}}_{R^{(k)}}$ denote the vector consisting of all components $\hat{\boldsymbol{\alpha}}_{\mathrm{LS}}$ in $R^{(k)}$.
7. Form a steering matrix $\Phi_{\alpha}^{(k)}$ by deleting all rows and columns in the matrix $\hat{\boldsymbol{\alpha}}_{R^{(k)}}$ specified by $P^{(k)}$.
8. Calculate $\lambda_{\max}^{(k)} = \left(\Phi_{\alpha}^{(k)}\right)^{-1} \hat{\boldsymbol{\alpha}}_{R^{(k)}}$. If all the components in $\lambda_{\max}^{(k)}$ are negative, go to step 13; otherwise, continue.
9. Calculate $\lambda_{\max}^{(k)} = \max \lambda_{j}^{(k)}$ and move its index in $R^{(k)}$ to $P^{(k)}$.
10. Form another matrix $\Psi_{\lambda}^{(k)}$ by deleting every column of $\left(\mathbf{M}^{T}\mathbf{M}\right)^{-1}$ specified by $P^{(k)}$.
11. Set $\hat{\boldsymbol{\alpha}}_{S^{(k)}} = \hat{\boldsymbol{\alpha}}_{LS} - \Psi_{\lambda}^{(k)} \lambda^{(k)}$.
12. If any component of $\hat{\boldsymbol{\alpha}}_{S^{(k)}}$ in $S^{(k)}$ is negative, then move it from $P^{(k)}$ to $R^{(k)}$ and go to step 6.
13. Form another matrix $\Psi_{\lambda}^{(k)}$ by deleting every column of $\left(\mathbf{M}^{T}\mathbf{M}\right)^{-1}$ specified by $P^{(k)}$.
14. Set $\hat{\boldsymbol{\alpha}}_{NCLS}^{(k)} = \hat{\boldsymbol{\alpha}}_{LS} - \Psi_{\lambda}^{(k)} \lambda^{(k)}$. Go to step 3.

7.4 ORNL EMAT PIG system SCC detection.

ORNL uses EMATs configured in "through-transmission mode" for SCC detection. In through-transmission mode, the transmitted wave is generated by one EMAT and received by another. Hence, independent of the location of the flaws, the ultrasonic waveform arrives at the receiver within a fixed time window since the distance between the receiver and the transmitter does not change. In "pulse-echo" mode, a single EMAT acts as both the transmitter and the receiver. The reflected signal is what is collected and analyzed. The characteristics of the signal received will be dependent on the location of the flaw from the transmitter. This dependency will cause a phase shift and attenuation of the signal. Hence, the pulse-echo mode is more difficult to implement for a pipe inspection gauge (PIG) that is translating through a pipe. To simplify the flaw analysis, only "through-transmission" mode was used in this project. Later on, to clearly identify the location of the flaws on the circumference of a pipe and obtain another signal from the same flaw location, "pulse-echo" mode might be incorporated into the design along with "through-transmission."

The pipeline industry is interested in detecting SCCs in transmission pipelines because the larger-diameter pipes carry large fuel volumes and the potential for greater damage exists when a pipe failure occurs. The ORNL EMATs are configured to detect flaws in 30-inch pipes. Figure 37 is a photo of the EMAT-based pipe test equipment. The main body of the test fixture is made of 80/20® aluminum and travels within the pipe on roller-blade wheels. The pair of EMATs that act as the sensing unit are attached to the frame. The EMATs have a pre-adjusted standoff distance from the pipe inside diameter of about 0.010–inch that is maintained by using a set of small roller wheels located on the sensor head mount. Independently mounted springs also allow the sensors to negotiate uneven surfaces of the pipe without damaging the EMAT head while maintaining distance to the inside wall surface. A resolver is used to measure the distance traveled by the inspection system while traveling inside the pipe. The circumferential separation between the transmitter and the receiver EMAT can be adjusted, and the current setting of 8 inches ensures that the excitation signal does not overlap with the transmitted chirp signal. To ensure that the PIG does not rotate circumferentially while traveling inside the pipe, a counterbalance weight is used that can be adjusted to make the PIG travel in a straight line.

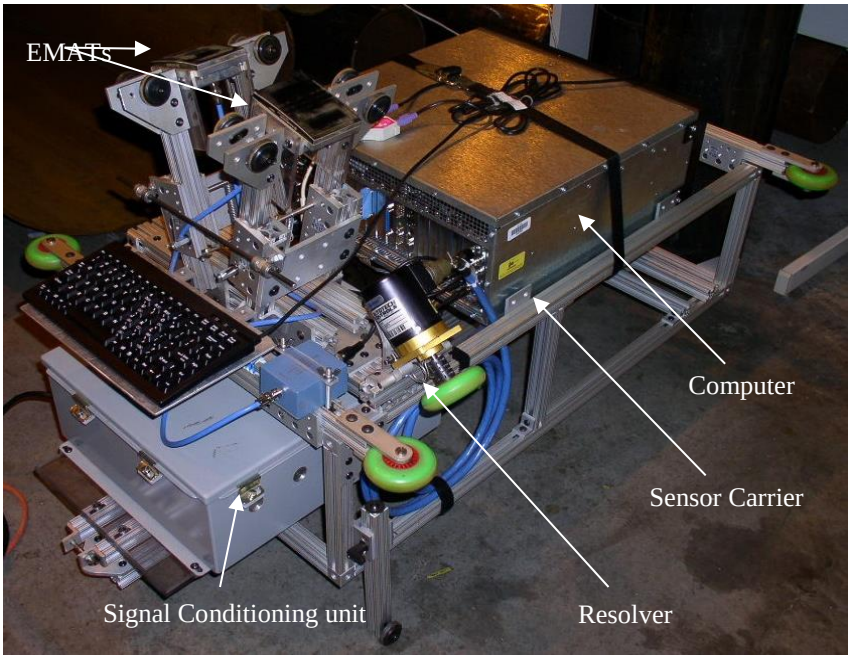

Fig. 37 ORNL PIG with EMAT sensors for inspecting a 30-inch diameter pipe.